Journal of
*Marine Science
and Engineering*

MDPI

Article

Mediterranean Marine Heatwaves: Atmospheric Drivers and Ocean Feedback

Cadan Plasa, Nikolaos Skliris * and Ligin Joseph

School of Ocean and Earth Science, University of Southampton, Southampton SO14 3ZH, UK; cip1u24@soton.ac.uk (C.P.)
* Correspondence: n.skliris@soton.ac.uk

Abstract

The influence of air–sea heat fluxes on the evolution of marine heatwaves (MHWs) in the Mediterranean was examined over the 1982–2024 summer periods. MHW detection was performed on detrended sea surface temperatures (SSTs), and the application of a minimum spatial coverage threshold of 15% of the Mediterranean Basin provided a catalogue of the most extreme MHW events. Analysis of composite surface flux anomalies shows that latent heat flux (LHF) anomalies dominate the contribution of the air–sea heat flux budget to MHW variability, with negative LHF anomalies before an event and positive LHF anomalies after an event. An alternative MHW detection method which defines MHW events from time series of the principal components (PCs) of MHW intensity was used. This method revealed distinct atmospheric patterns associated with the different phases of an MHW event. Before an MHW event, weakened winds reduce outgoing LHF, trapping heat within the ocean. After an MHW event, a steepening humidity gradient and strengthened winds increase outgoing LHF and heat release into the atmosphere. These results highlight the significant role that LHF plays in the interactions between MHW events and the atmosphere, and the contrasting contributions of wind speed and humidity gradient during MHW onset and decline.

Keywords: Mediterranean Sea; marine heatwaves; heat flux; sea surface temperature

1. Introduction

The Mediterranean Sea is a climate change “hotspot”, with an annual sea surface temperature (SST) trend estimated to be between 0.034 and 0.041 °C/year [1], more than twice the global rate of 0.015 °C/year [2], which is continuing to accelerate into the 21st century [3]. This makes the Mediterranean Sea particularly prone to periods of anomalously high SSTs, known as marine heatwaves (MHWs). These can occur both at the surface and at the subsurface, with the potential to permeate up to two thousand metres into the water column [4].

MHWs can have devastating ecological impacts. This is particularly true for the Mediterranean Sea, which is a uniquely biodiverse region, containing an estimated 17,000 unique species [5]. These provide crucial ecosystem services to the 150 million people who form the coastal communities around the Mediterranean, many of whom depend on the already over-exploited marine ecosystems for food and income [6]. The correlation between ecological mass mortality events and MHWs has been well-documented [7], as have potential relationships between MHWs and heat-stress related conditions across a wide

Check for updates

Received: 30 January 2026
Revised: 28 February 2026
Accepted: 4 March 2026
Published: 8 March 2026

https://doi.org/10.3390/jmse14050509

range of taxa from seagrass [8] to corals [9]. MHWs also directly impact the Mediterranean food chain at all levels, from primary productivity [10] to aqua-cultural fish stocks [11].

The extreme build-up of heat within the ocean during an MHW also has a strong potential to influence and be influenced by the dynamics of the atmosphere. This has significant consequences for the Mediterranean on both local and basin-wide scales. For example, the extreme evaporation associated with an MHW was linked to the unusually rapid intensification of cyclone Ianos [12]. A similar pattern was found for medicane Scott, with elevated evaporation over an MHW potentially contributing to its formation [13]. This has the potential to lead to a positive feedback loop, since medicane intensification leads to stronger winds [14], which further promote evaporation from the sea surface. On top of this, atmospheric heatwaves and MHWs have been found to become increasingly concurrent, with atmospheric heatwaves generally leading to a local intensification of the MHW event [15]. This has been suggested to be the result of the exchange of heat fluxes between the ocean and the atmosphere [16]. A link has also been found between MHW and supercell intensity [17], as well as between MHW intensity and hail-size index, with the suggestion that a concurrent MHW increased the severity of an extreme hail event in Spain in 2022 [18]. These findings demonstrate the varied impacts of MHWs on the atmosphere. In particular, high SSTs and increased evaporation frequently provide the physical link between an MHW in the ocean and its influence on the atmosphere.

Comparing results of separate works on MHWs is difficult because there is no universally accepted definition of what constitutes an MHW. Instead, most studies adapt a framework first proposed by Hobday et al. [19], where SSTs must exceed the 90th percentile of a given reference climatology for 5 or more consecutive days for an event to be considered an MHW. This definition was successful at unifying the general approach to MHWs and underpins all modern works within the field, including the results presented here. However, this definition has been subject to criticism. Pastor et al. [20] note that since the definition has no condition on minimum spatial extent, it risks the inclusion of brief, isolated events which have little impact. Subsequent studies have conducted experiments by varying the temperature threshold and minimum spatial extent required for an MHW to occur, with the goal of identifying only the most extreme events [21].

A significant debate surrounds the reference climatology in the Hobday definition. By keeping the baseline period fixed, temperatures further into the future become increasingly likely to exceed the 90th percentile threshold. When temperatures are projected to the end of the 21st century under high-emission scenarios, this leads to a Mediterranean almost entirely saturated by MHWs [1]. This threatens the robustness of the definition of an MHW—temperatures cannot be understood as "anomalously warm" if they are "anomalously warm" everywhere, at all times. On shorter time scales, the warming temperature trend drives trends across all measurements of MHWs, including their intensity, duration and frequency [22,23], as the most extreme temperatures shift further beyond their percentile threshold.

While the Hobday approach adequately conveys the threat that an MHW provides to organisms with low adaptability to global warming [24], it is incompatible with the definition of an MHW as an extreme event. One approach which addresses this is the use of a moving baseline, where the reference climatology is shifted forward in time as the years of interest are progressively further in the future. This ensures that the probability of MHW occurrence is as fixed as it possibly can be and thus represents a true statistical extreme [25]. Another approach is simply removing the background warming trend before performing MHW detection. This has been applied to the Mediterranean, where no statistically significant trend in MHW statistics was found after detrending [26], with significant trends in all MHW statistics having been found for the raw data. An advantage of the detrended approach is that for earlier time periods, it does not require data which extend past the range of the study period. This is particularly useful for earlier years where a moving baseline requires the use of pre-satellite-era SST data. For this study, which focuses on MHW interactions with the atmosphere, detrending the SST distribution allows for the isolation of MHW events associated with short-term atmospheric variability rather than long-term warming.

Analysis of the drivers of MHW events in the Mediterranean constitutes a significant knowledge gap [1], with most studies concentrating on individual events. An integrated view was presented by Denaxa et al. [27], who found that air–sea heat flux anomalies dominated the MHW heat budget of 44% of MHW events in the onset phase and of 17% of MHW events in the decline phase. This would indicate that oceanic processes play a larger role than heat flux in driving MHW events. However, the investigation by Denaxa et al. [27] used the Hobday definition in its original form, with a fixed baseline and no minimum spatial extent. On a larger spatial scale, a recent investigation grouped MHW points together via a clustering algorithm to identify "macroevents" [28]. This enforced a stricter criterion for MHW detection whilst also incorporating a fixed baseline. Their work identified anticyclonic weather patterns and decreased wind speed as major causes of Mediterranean MHW onset.

While these studies provide great insights into MHW dynamics, there remains a gap regarding several elements of MHW interactions at the air–sea interface. Firstly, while some improvements have been made by Bonino et al. [28], their work focused on synoptic weather patterns, and a detailed investigation of air–sea heat fluxes and their drivers, such as their magnitude, their temporal evolution, and an interpretation of their relationship to one another, has yet to be made. Secondly, while the humidity gradient undoubtedly contributes to latent heat flux (LHF) (as per Equation (3)), the role of the humidity gradient before and after an event has yet to be investigated. Additionally, analysis which synthesises these relationships across only the most extreme events has yet to be performed—while Bonino et al. [28] incorporated a spatial element into their definition, they still identified 123 events. In contrast, investigations into the most severe events in the Mediterranean over the same time period typically find 20–30 events [26,29]. There is a need to integrate all of these factors, across both MHW onset and decay, for a clearer picture of how air–sea interactions can drive MHW variability.

The aim of this study is to address the above concerns by constructing a detailed assessment of the role of air–sea interactions in driving MHW onset and decay, across a new catalogue of the most extreme summertime MHW events in the Mediterranean. This includes determining the major contributors to the air–sea heat flux budget before and after an event, their associated atmospheric patterns, and the response of SSTs to these changes. Section 2 outlines the data and the MHW detection methods used in this study. Section 3.1 describes SST and LHF trends over the study period, which form the foundation of the SST detrending process investigated in Section 3.2. In Sections 3.3 and 3.4, extreme MHWs are catalogued across the study period. In Section 3.5, drivers of MHWs are analysed for the 2003 event (Section 3.5.1) and then aggregated over all events in Section 3.5.2. Section 3.6 presents results from a separate MHW detection method based on empirical orthogonal function (EOF) analysis. These results, and the strengths and weaknesses of both approaches, are discussed in Section 4.

2. Materials and Methods

2.1. Data

SST data were retrieved from the Optimum Interpolation Sea Surface Temperature (OISST) dataset [30]. OISST compiles records from different observational platforms (e.g., satellites and Argo floats) to provide a three-dimensional set of high-resolution SST data aligned on a global 0.25° × 0.25° latitude/longitude grid. The data give daily readings across the entirety of the study period, from 1982 to 2024. Air–sea heat fluxes, 10 m wind speed, 2 m air temperature, surface pressure and 2 m specific humidity were retrieved from the ECMWF's ERA5 dataset [31]. SST and surface pressure were then used to calculate saturation humidity at the sea surface. ERA5 consists of high-resolution 0.25° × 0.25° gridded reanalysis data, which combine observations with state-of-the-art modelling results. As with OISST, ERA5 provided daily data over the whole study period.

2.2. The Mediterranean Basin

Since the drivers and character of Mediterranean MHWs vary regionally, it is often informative to divide the Mediterranean into sub-regions when performing MHW analysis [32]. For this work, the Mediterranean was divided into 4 sub-regions, following the division by Pastor et al. [20], which divides the Mediterranean into regions with the most similar patterns of warming and circulation.

These regions are shown in Figure 1 and are referred to as western Mediterranean (WMED), central Mediterranean (CMED), Adriatic Sea, and eastern Mediterranean (EMED) throughout the rest of this work. This division was achieved in practice by applying a polygon mask representing each sub-region to the datasets.

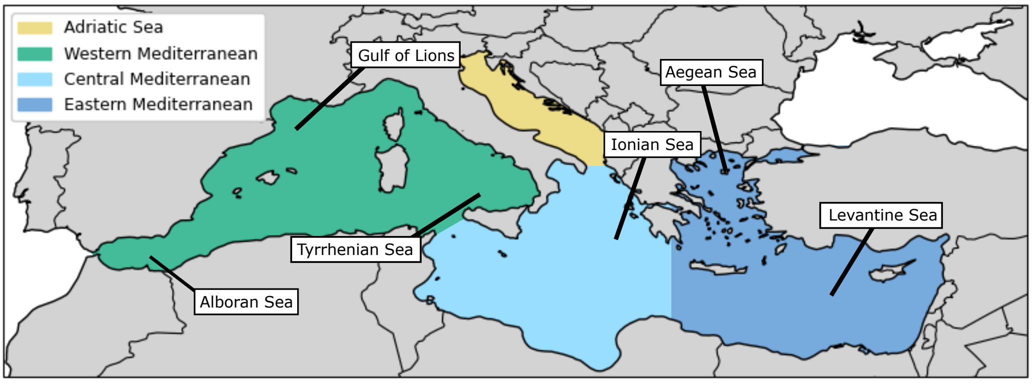

Figure 1. The division of the Mediterranean Basin into distinct sub-regions as used by this work, following the division by Pastor et al. [20]. Names of key regions are annotated in black.

2.3. Trend Detection

Time series of climatic data can be modelled by the following equation [33]:

$$Y(t) = T(t) + S(t) + e(t) \tag{1}$$

where $Y(t)$ represents the measured value at a specific time t, $T(t)$ represents the long-term trend, $S(t)$ represents the seasonal cycle in the data and $e(t)$ represents the residual components of the signal. To isolate only the long-term trend in the data, the seasonal and residual components were removed with the use of the seasonal_decompose function from the statsmodels package (v.0.14.2) in Python (v.3.13) [34], which applies a simple low-pass filter to split the signal into trend, seasonal and residual components. To obtain the spatial map of trends in Section 3.1, linear regression was then performed solely on the trend component of the resulting time series, across the 1982–2024 period and for each grid point. Trend significance at each grid point was then assessed using a two-sided hypothesis test at the 5% significance level. The regional trends reported in Section 3.1 were obtained from the same method, but with the time series averaged over each region. By subtracting the established trend from each grid point, the detrended SST data used for MHW detection throughout Sections 3.2–3.6 is obtained.

2.4. The MHW Heat Budget

The air–sea heat flux budget is given by:

$$Q_{net} = Q_{LW} + Q_{SW} + Q_{SHF} + Q_{LHF} \tag{2}$$

where Q_{LW} represents net longwave radiation, Q_{SW} represents net shortwave radiation, and Q_{SHF} represents the net exchange of heat through conductive processes (sensible heat flux). Q_{LHF} is the net contribution to heat exchange from evaporative processes, known as LHF. LHF accounts for as much as 80% of air–sea heat flux anomalies during an MHW event [35] and is often parameterised as:

$$Q_{LHF} \approx \rho L_e c_e W \Delta q \tag{3}$$

where ρ is the density of seawater, L_e is the latent heat of vaporisation, c_e is the turbulent exchange coefficient, W is wind speed and Δq is the humidity gradient, which is defined as the difference between the specific humidity at 2 m and the saturation humidity at the sea surface [36]. All fluxes are defined as positive upward in this study, so a positive value indicates the loss of heat from the ocean to the atmosphere. It should be stressed that Equation (3) is an approximation, but it is nevertheless illuminating—LHF is roughly proportional to wind speed and the humidity gradient. This motivates the choice of these variables when investigating drivers of LHF anomalies in Section 3.5.

2.5. MHW Detection

The baseline climatology for this study comprises pixel-wise daily average SST values over the 1982–2024 period. Following Hobday et al. [19], we define the climatological mean over this period as:

$$T_m(j) = \frac{1}{43} \sum_{y=1982}^{2024} \sum_{d=j-5}^{j+5} \frac{T(y,d)}{11} \tag{4}$$

where $T_m(j)$ is the climatological mean for day j and $T(y,d)$ is the SST value on day d of year y. The second sum represents the mean temperature over an 11-day window, smoothing out short-term temperature variations. The first sum represents the mean of these values across the baseline period. A separate mean is computed for each gridded data point, and the pixel-wise difference between daily SSTs and their climatological mean defines the SST anomaly. The temperature threshold $T_{90}(j)$ for day j is given by $T_{90}(j) = P_{90}(X)$ where P_{90} is the 90th percentile and X is the subset of all temperatures, given by:

$$X = \{T(y,d) |\, 1982 \leq y \leq 2024,\ j-5 \leq d \leq j+5\}. \tag{5}$$

This is similarly computed separately for each gridded data point. An MHW occurs when temperatures at a point exceed this threshold for 5 or more consecutive days.

Throughout the literature, MHW is often used to refer to events at individual grid points, as well as the collection of MHW grid points over a specific period, e.g., "The 2003 MHW". To avoid confusion, this study refers to an individual grid point experiencing MHW conditions as an "MHW". The term "MHW event" is reserved only for groups of MHWs whose total area exceeds a minimum spatial requirement of 15% of the Mediterranean, for 5 or more days. An MHW event thus represents groups of MHWs whose collective impact is the most extreme. For both MHWs and MHW events, gaps of up to 2 days between consecutive periods of 5 days or longer are permissible, following Hobday et al. [19].

The MHW detection window is chosen to extend from 31 May to the 26 September of each year, encompassing the summer period, when MHW activity is the most intense [20]. In the case where an MHW event occurs within the window and extends past its end date, the window is extended until the MHW event declines.

The MHW detection criteria at an individual grid point are demonstrated in Figure 2. Two clear periods of MHW conditions can be seen, with the first occurring between 14 July and 27 July and the second occurring between 6 August and 6 September. These are counted as two separate MHWs, as the period between them when SSTs drop below the temperature threshold lasts longer than 2 days.

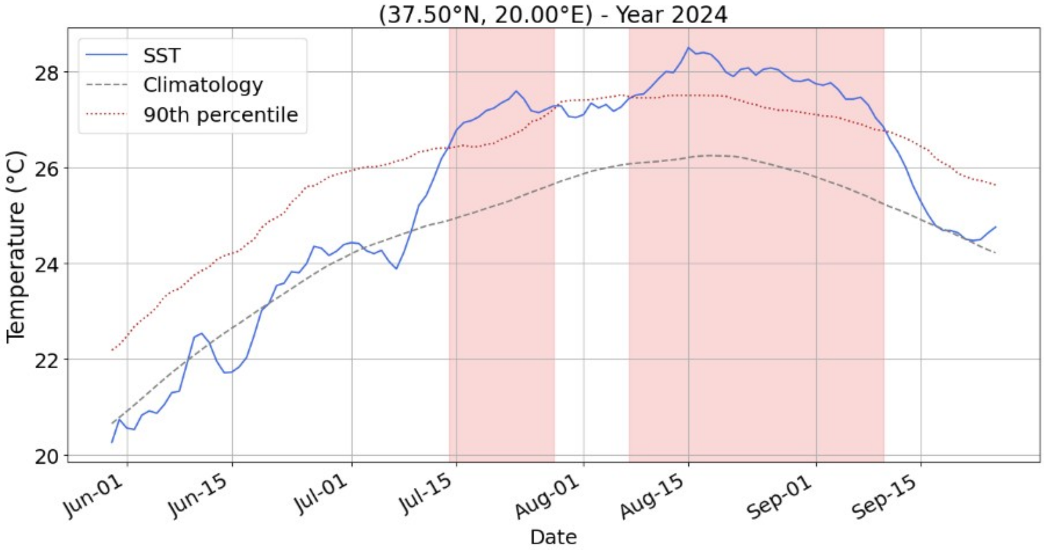

Figure 2. MHW detection at 37.5° N, 20° E over the 31 May–26 September period in 2024. The baseline climatology is shown in grey, with the 90th percentile threshold in red. The red shading indicates regions where the SST (sea surface temperature) satisfies MHW conditions for 5 or more consecutive days.

2.6. MHW Metrics

To assess the characteristics of MHWs, this study adopts several metrics first defined by Hobday et al. [19]:

- The intensity of an MHW on a given day is the SST anomaly at that point.
- The mean intensity of an MHW or MHW event is the average intensity value experienced over its duration.
- The maximum intensity of an MHW or MHW event is the greatest intensity value reached over its duration.
- The cumulative intensity of an MHW is defined as the sum of the daily intensities over its duration.
- The number of MHW days is defined as the total number of days during which a given point experienced an MHW.

While cumulative intensity is a suitable indicator of the impact of an MHW, an equivalent metric for an MHW event should ideally contain some form of information regarding its spatial extent. The concept of MHW event severity suitably conveys this information [29]. MHW event severity is the product of the cumulative intensity of each MHW and its spatial extent in km^2, summed over all the MHWs which constitute the event.

2.7. EOF Analysis of MHW Intensity

EOF analysis is a technique that decomposes climate data into individual, orthogonal patterns (modes) which together explain the majority of its variability. Each mode has a spatial component (EOF) as well as a time series, known as the principal component (PC), which contains information on how intense that spatial pattern is at a particular time. The advantage of this technique is that the arrangement of the spatial pattern does not evolve over time, varying only in sign and magnitude. Section 3.6 leverages these advantages to analyse the air–sea interactions of MHWs more robustly than through the use of traditional methods.

EOF analysis is performed on MHW intensities over the course of the study period. Only modes which explain a significant proportion of the variance in the MHW intensity signal (they explain approximately >5% of the variance) are kept for the analysis. Normalised time series of each PC are then produced. EOF analysis is performed in Python (v.3.13) using the xeofs package (v.3.0.4) [37].

As the MHW intensity signal is split into its PCs, a new way of identifying extreme signals (analogous to MHW events) must be introduced. The definition of a PC MHW event is adapted from Joseph et al. [38] to be a period of 10 or more days for which the normalised score of a PC exceeds the 90th percentile for that day. For a given PC, the 90th percentile threshold is defined as in Equation (5) but with the substitution of PC scores for SST values. A 10-day requirement is introduced here rather than the original 5-day requirement to prevent the overlap of the periods before and after a PC MHW. For PCs whose time series have negative values, an additional set of PC MHW events is obtained by choosing periods for which the PC drops below its 10th percentile. The start and end dates of PC events for each component are then used to produce composite time series of atmospheric and oceanic anomalies before and after a PC MHW event, in the same way as for the traditional MHW events as described above.

3. Results

3.1. SST and LHF Trends

As the MHW detection method relies on detrended SST data, the first step towards this goal is identifying SST trends. Trends in SSTs and LHFs across the study period are shown in Figure 3. There is a statistically significant positive SST trend throughout the Mediterranean over the course of the study period. SST trends are the strongest around the Gulf of Lions, the Adriatic Sea and some parts of the Levantine Basin. In contrast the SST trends in the CMED and the Aegean Sea were much smaller, but p-values were still significant below the 5% significance level. The pattern of LHF follows the spatial pattern of SST trends in some areas, with generally low values throughout the CMED. There are however distinct differences in the Gulf of Lions, where LHF values are low compared with the relatively high SST trend values. The greatest LHF trend values are found in the eastern Levantine Basin, reaching values as high as 1 $W/m^2/year$. Some areas, such as the eastern Aegean Sea, present statistically insignificant LHF trends.

Area-averaged (over different divisions of the Mediterranean Basin) SST yearly series and trends are presented in Figure 4. Uncertainties are large, ranging between 10 and 20% of the trend value, making it difficult to distinguish statistically significant differences among sub-basins. One comparison that can be made is that the WMED trends are, on average, larger than the CMED trends. Figure 4 also plots average SST values across the study period for each year. Raw temperatures are typically the smallest in the WMED and the largest in the CMED. For the CMED and WMED, large peaks in average SSTs occur in 1994, 2003, and 2022. This signal is large enough to be seen when averaged across all sub-regions in the time series for the whole Mediterranean. Area-averaged SST trends over all days between 1982 and 2024 are shown in Figure A1.

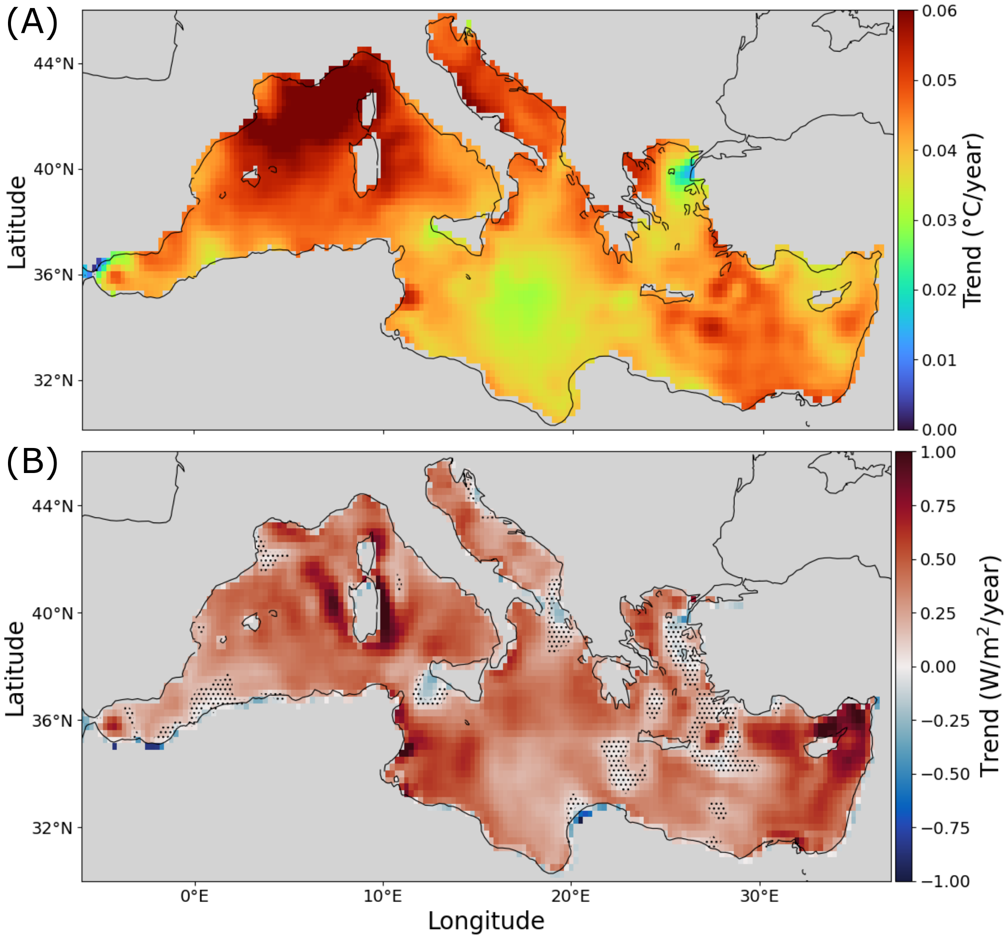

Figure 3. (**A**) SST trends and (**B**) latent heat flux (LHF) trends between 31 May and 26 September over the 1982–2024 period from the OISST dataset. Regions of trends which were not significant below the 5% significance level are shown by black dots.

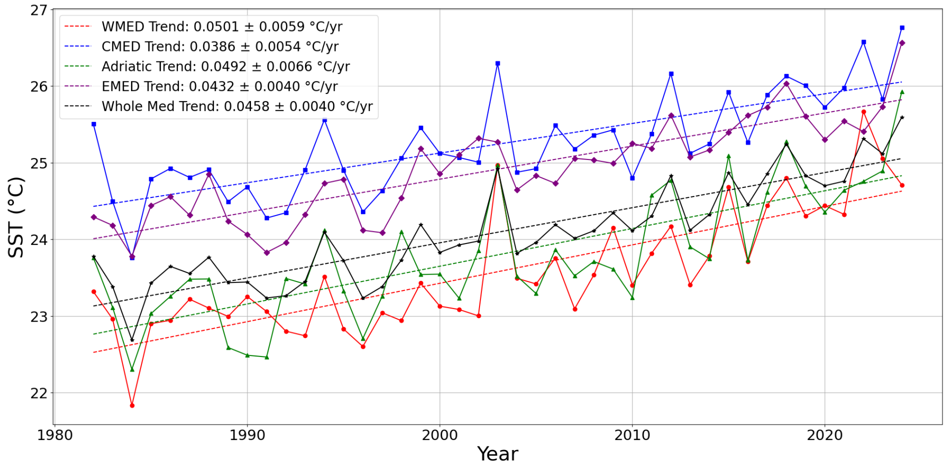

Figure 4. Time series of annually averaged SST values over the 31 May–26 September period from 1982 to 2024. Coloured solid lines show the time series for each sub-region. The linear fit plotted was calculated from all daily data over this period. Trends are split into four sub-regions as outlined in Section 2.2.

3.2. Detrending

Once the SST trends were identified, raw SST values were detrended. The effects of detrending raw SST values on the calculated SST anomalies are presented in Figure 5. Throughout all sub-regions, the mean of the raw SST anomaly distribution is higher for the 1982–2002 period than the 2003–2024 period. The most extreme effect can be seen in the WMED, where the difference in the means of the two distributions was 0.8 °C. This is also the region which experienced the strongest SST trends overall. The difference was the lowest in the CMED, in line with the region of the weakest SST trends. The difference in standard deviation was the largest in the Adriatic Sea, where the distribution of raw SSTs also deviated from the relatively symmetric structure experienced by other distributions.

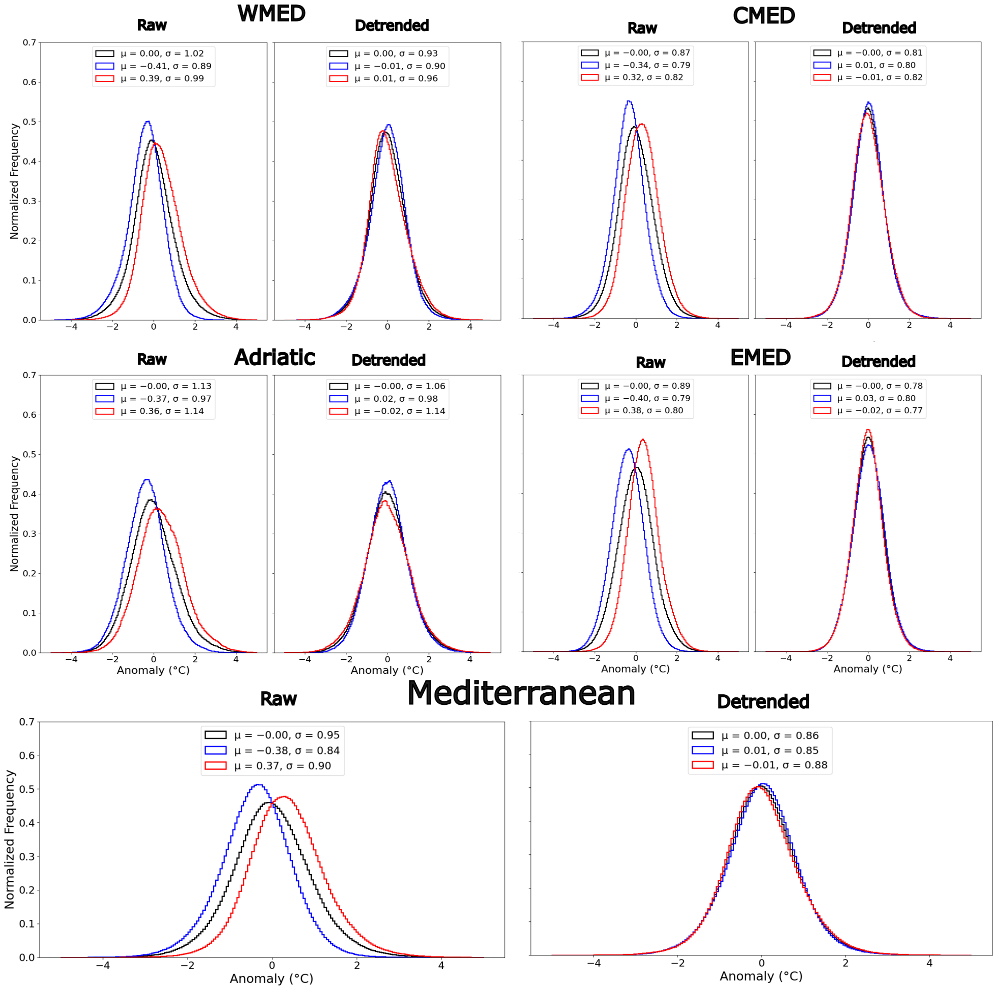

Figure 5. Probability density distributions of SST anomalies for raw and detrended SST data. SST values have been detrended by subtracting a linear fit to their trend component. Blue lines represent the distribution for the 1982–2002 period, whereas red lines represent the distribution over the 2003–2024 period. The distribution over the entire 1982–2024 study period is shown in black. Distributions are presented for individual sub-regions following the division in Section 2.2 as well as the whole of the Mediterranean.

In all regions, the distributions of SST anomalies shift closer together after the detrending process. This effect is greatest for the WMED and CMED, where the means of the SST anomaly distributions shifted towards one another for both the 1982–2002 and 2003–2024 periods. The detrending process was slightly less effective in the Adriatic Sea and EMED. These deviations did not have a major impact on the SST trends when assessed across all basins, with a difference of 0.02 °C between the means of the 1982–2002 and 2003–2024 distributions after the detrending process. In all cases, the standard deviation changed little for the distributions which were split into an earlier and later period. In contrast the total standard deviation of the distributions for all years changed more significantly, with the greatest change being experienced in the EMED. The plot of the detrended distributions in Figure 5 correspondingly becomes more sharply peaked. The overall effect of the detrending process was that the distributions over the two periods overlapped more closely, with a narrower peak when considered over the entire study period.

3.3. MHW Statistics

After detrending the raw SST values, MHW detection was performed at individual grid points throughout the Mediterranean. A comparison between spatial maps of key MHW metrics using the raw and detrended SST distributions is shown in Figure 6. For mean, maximum and cumulative intensity, the spatial distribution of MHW metrics has a similar pattern in both the raw and detrended cases, but with significantly smaller magnitude for the detrended case.

For the raw SSTs, mean intensity displays a clear northeast to southwest gradient, with the highest mean intensities in the northern Adriatic Sea and around the southern coast of France. Throughout the Gulf of Lions and the coasts of Italy and Greece, mean intensity decreases on an eastward gradient, reaching its lowest values in the EMED and Levantine Sea. Detrended mean intensities follow a similar pattern, albeit with a slightly decreased amplitude and a stronger gradient. The difference in mean intensities between the two·plots shows a decrease in mean intensity across the basin, although some small sections such as the central Aegean Sea experience no difference. Mean intensity experienced the greatest decrease in the EMED, where intensity decreased by more than 0.5 °C.

Maximum intensity is the greatest for the raw SST values along the southern coast of France. Maximum intensity follows a near identical pattern to mean intensity for the raw SST values, sharply decreasing on a southeasterly gradient between the WMED and the southern parts of the CMED and EMED. The detrended maximum intensity values are the least affected of all four examined metrics, following a very similar spatial pattern to the maximum intensity of the raw SST MHWs. Throughout much of the CMED, as well as the central Aegean Sea, maximum intensity values even experience an increase, particularly along the northern coast of Africa.

As with the other intensity metrics, cumulative intensity reaches its maximum value in the Gulf of Lions for both the raw and detrended cases. These values decrease moving southwards, albeit along a shallower gradient than the intensity metrics, with large cumulative intensities spread throughout the Adriatic Sea. Once again the detrended cumulative intensity follows a similar pattern, although regions such as the EMED and Gulf of Lions show a sharp decrease.

The spatial pattern of total MHW days is noticeably different from the spatial pattern of the other three metrics, with no individual sub-region consistently experiencing the greatest values. For the raw SSTs, the largest values are experienced throughout the EMED, WMED and CMED, although they are noticeably absent from the Aegean Sea, which experienced relatively few MHW days across the study period. For the detrended case, the greatest values are reached in a smaller region spanning around the CMED. The EMED shows the greatest decline of any region after detrending.

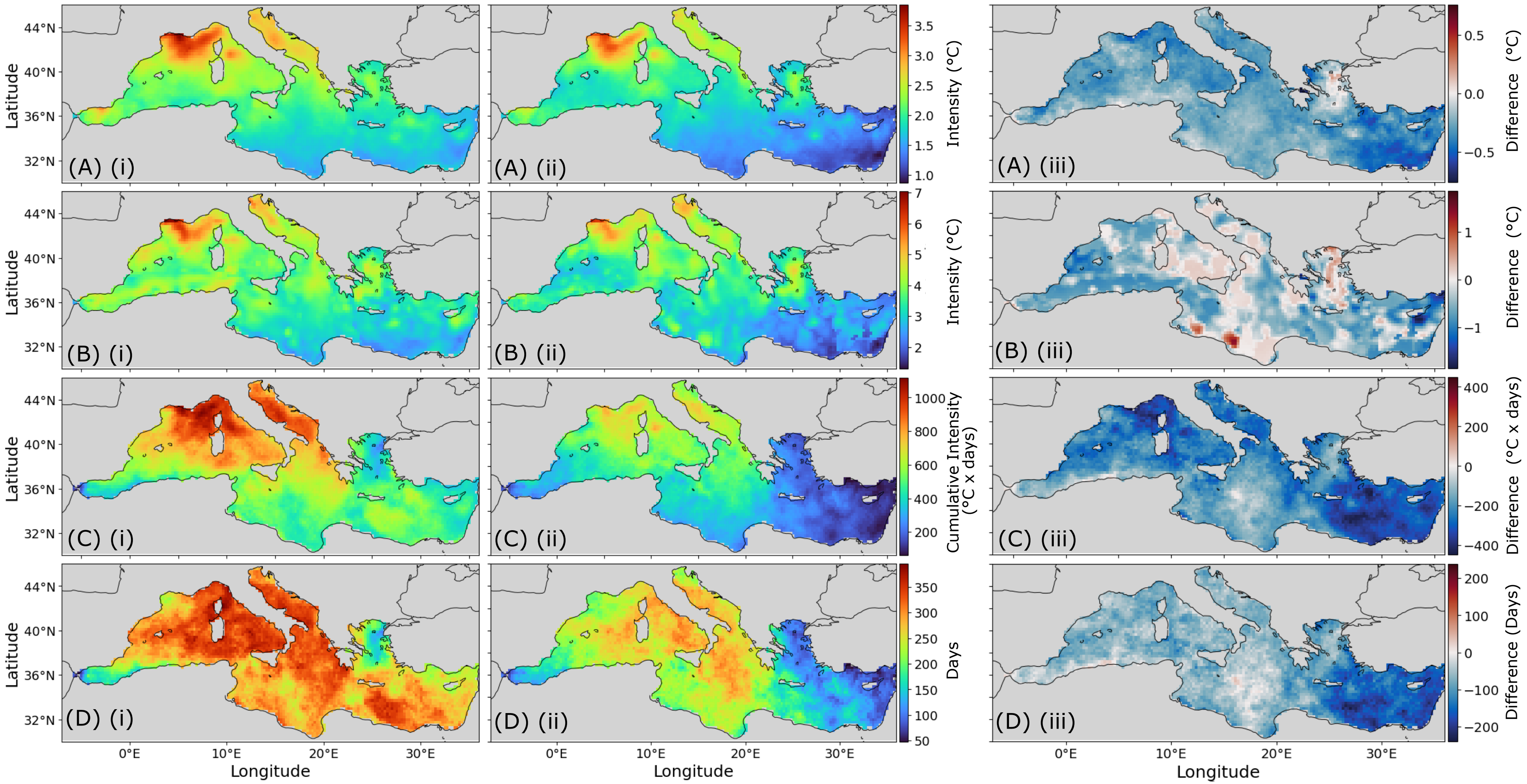

Figure 6. MHW statistics for the Mediterranean between 31 May and 26 September over the 1982–2024 period. Values are calculated pixel-wise. Mean intensity (°C) (**A**) is the average temperature anomaly during an MHW, and maximum intensity (°C) (**B**) is the greatest temperature anomaly reached during any MHW. Cumulative intensity (°C days) (**C**) is MHW intensity summed over all days which experienced an MHW, and the number of MHW days (**D**) is the total number of days in which temperatures exceeded the MHW threshold. Metrics were calculated for the raw (**i**) and detrended (**ii**) SST data, with the difference between the two shown alongside them (**iii**).

3.4. MHW Events

After MHWs were detected at individual grid points across the study period, MHW events were detected following the application of a minimum spatial threshold, as outlined in Section 2.5. In total, 35 events were detected for the raw SST data, and 36 events were detected for the detrended SST data. Table 1 displays the subset of these events whose durations last 10 days or longer. This highlights the most impactful events.

The durations of the detected events are highly variable, ranging between 16 and 94 days in total. The longest-lasting event was the 2003 event. Mean intensities ranged from 1.52 °C to 2.40 °C, with the greatest mean intensity value experienced in the 2006 event. Maximum intensity varied between 3.39 °C, experienced in the 2020 event, and 5.55 °C, which was reached during the second event of 2018. Severity was the most variable metric, ranging between 16 × 10^6 °C days km^2 (1999 event) and 243 × 10^6 °C days km^2 (2003 event). The 2003 event stands out as particularly severe, experiencing a severity over double that of the next greatest value, which was 111 × 10^6 °C days km^2, experienced in the 2024 event. This is because the choice of a 15% spatial threshold and 90th percentile temperature threshold combines three 2003 events into one after the detrending process. This can be seen in Figure 7, where there are two 2003 events of medium strength for the raw SST data. Figure 8 reveals a third 2003 event for the raw data, which is not included in the above figure, as it lasted less than 10 days. The unusually large values of severity and duration for the detrended 2003 event relative to the values for the raw 2003 events are a consequence of the combination of these three events into one.

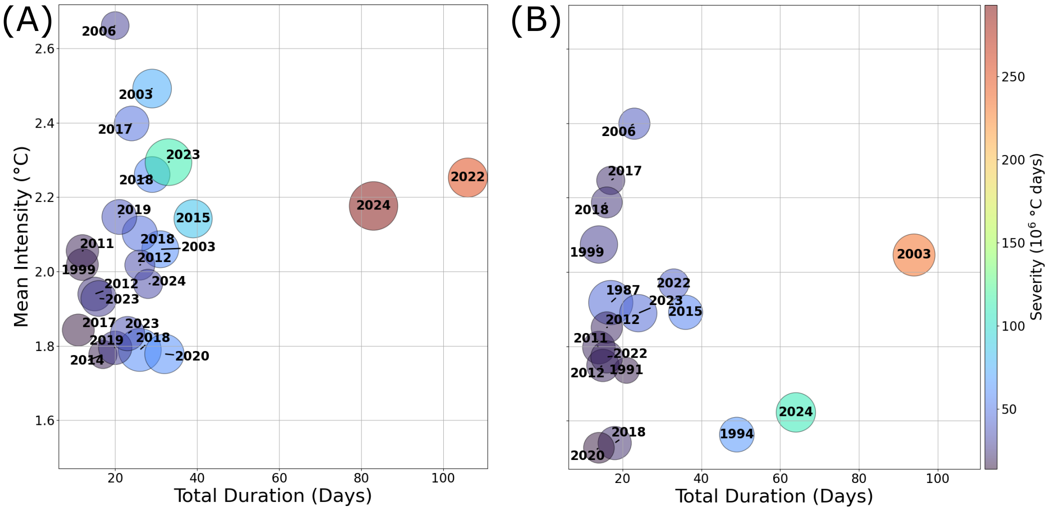

Figure 7. A comparison between MHW events which lasted longer than 10 days for the raw (**A**) and detrended (**B**) SST data. Detection was performed over dates between 31 May and 26 September in the 1982–2024 period. The year in which each MHW event occurred is annotated inside each corresponding bubble. The radius of each bubble corresponds to the mean spatial extent of the event, with a larger radius indicating a greater spatial extent and vice versa.

Table 1. A catalogue of MHW events which lasted longer than 10 days after detrending the OISST data. MHW detection was performed between 31 May and 26 September, although this range is extended for cases where an MHW event occurs within this period and continues past its end date. MHW events are ordered chronologically. Mean affected area was calculated as the average spatial extent of an event over its duration, expressed as a fraction of each sub-region's total area.

		MHW Statistics				Mean Affected Area (%)				
Start	**End**	**Duration (Days)**	**Mean Intensity (°C)**	**Maximum Intensity (°C)**	**Severity (10^6 °C Days km^2)**	**Med**	**WMED**	**CMED**	**Adriatic Sea**	**EMED**
19 Sep 1982	6 Oct 1982	18	1.69	3.43	24	30	16	54	80	15
10 Sep 1987	4 Oct 1987	25	1.84	4.18	59	51	72	52	74	20
4 Sep 1991	24 Sep 1991	21	1.73	3.77	17	18	53	0	0	0
3 Aug 1994	20 Sep 1994	49	1.56	4.00	64	33	23	54	51	22
25 Sep 1999	8 Oct 1999	14	1.47	3.64	16	30	20	43	55	27
4 Jun 2003	5 Sep 2003	94	2.04	5.26	243	48	63	64	48	18
12 Jul 2006	3 Aug 2006	23	2.40	5.42	37	27	61	19	3	0
8 Sep 2011	21 Sep 2011	14	1.80	4.10	19	29	26	29	97	18
1 Jul 2012	16 Jul 2012	16	1.85	4.06	20	27	14	40	90	16
16 Aug 2012	30 Aug 2012	15	1.75	4.23	19	28	54	12	25	14
15 Jul 2015	19 Aug 2015	36	1.89	4.6	55	32	27	31	64	30
11 Jun 2017	27 Jun 2017	17	2.25	4.82	21	22	53	4	10	3
29 Jul 2018	13 Aug 2018	16	2.19	5.55	23	26	48	7	58	12
7 Sep 2018	24 Sep 2018	18	1.54	3.61	21	30	26	53	56	9
12 Sep 2020	26 Sep 2020	15	1.52	3.39	15	26	27	16	50	26
15 Jul 2022	16 Aug 2022	33	1.97	4.51	41	25	62	13	0	0
2 Sep 2022	17 Sep 2022	16	1.77	3.80	20	28	65	18	2	1
12 Jul 2023	4 Aug 2023	24	1.88	3.96	44	38	34	51	38	30
13 Jul 2024	14 Sep 2024	64	1.62	4.73	111	42	18	64	68	43

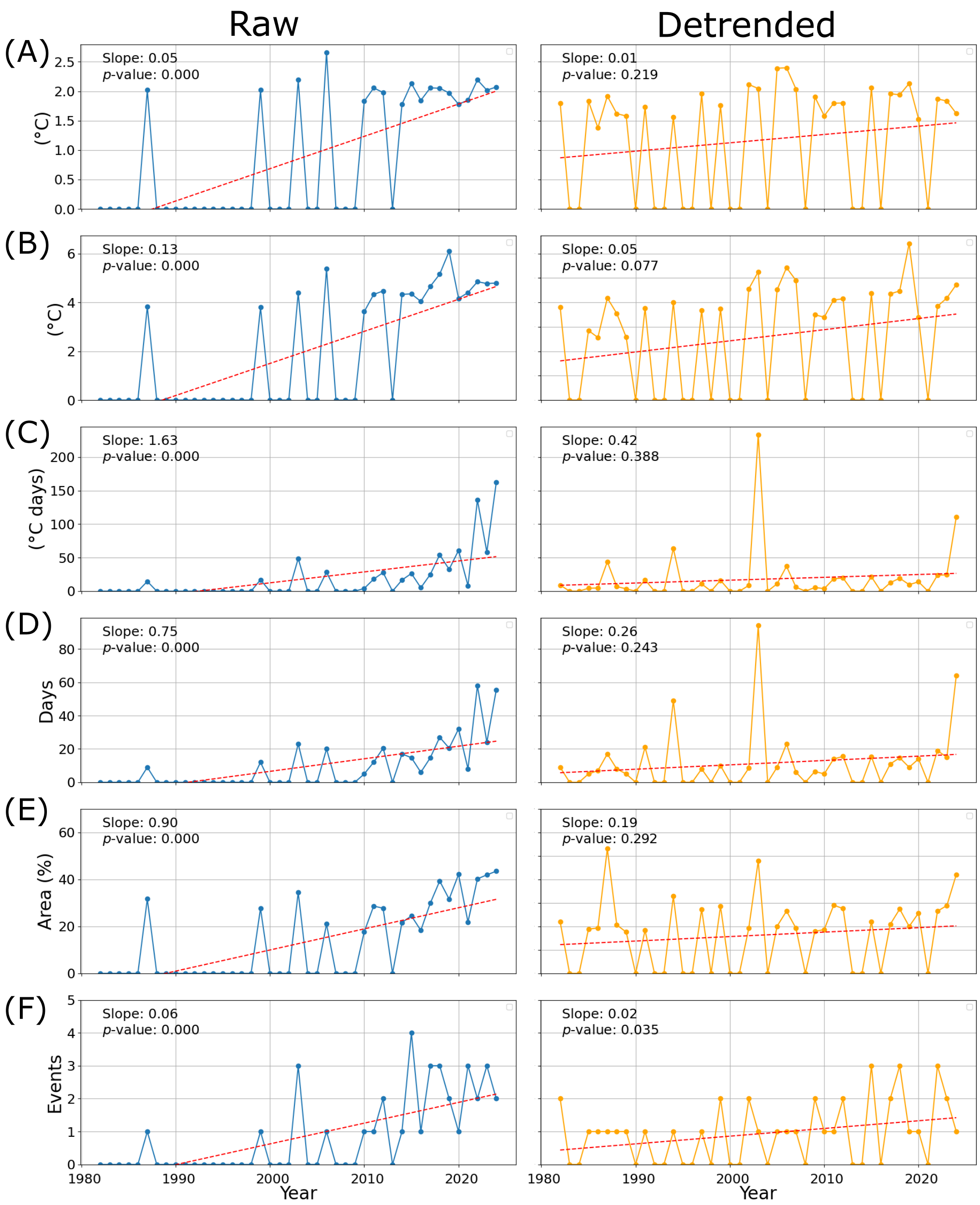

Figure 8. A comparison between annually averaged values of mean intensity (**A**), maximum intensity (**B**), cumulative intensity (**C**), MHW days (**D**), mean spatial extent (**E**) and number of events (**F**) for the raw and detrended OISST data, between 31 May and 26 September over the 1982–2024 period. Trend lines from a linear fit are plotted in red.

The mean affected area ranged from 18% (1991 event) to 48% (2003 event) of the Mediterranean Basin. The WMED experienced the most consistently high values, with the 1987 event affecting the largest mean area, spanning 72% of the region on average. The CMED was also significantly affected by MHWs, with as much as 64% being affected during the 2003 and 2024 events. The Adriatic Sea experienced the greatest maximum value of mean affected area, with the 2011 event affecting 97% of the region. However, there were still five events which affected below 10% of the Adriatic Sea on average. Of all sub-regions, the EMED experienced the lowest values of mean affected area, with values ranging from 0 to 43%. Six events affected below 10% of the EMED, and the EMED was entirely unaffected by the 1991, 2006 and lattermost 2022 event.

A comparison between MHW events detected for the raw and detrended distributions is shown in Figure 7. For the raw SST data, 2022 and 2024 were by far the events of the greatest severity. These events are still significant in the detrended case but are much less severe. In the detrended case, it is the 2003 event that was the most severe, followed by the 2024 event. Event duration has decreased across most of the later events for the detrended case but has increased for some of the earlier events, most notably the 2003 event, a result of the combination of multiple events into one, as described above.

Mean intensities also decrease across almost all detrended events, with the later events being the most severely impacted. Some of the earlier events, such as the 1999 event, experienced increases in mean intensity, although the effect is small. The mean spatial extent also decreases across all events in the detrended case, apart from in rare cases of the statistically most extreme events, such as in 2003. Another notable feature of Figure 7 is that several events which are absent when considering the raw SST data occur in the detrended case. These include the 1994 and 1999 events.

The trends in the annually averaged values of all MHW metrics are shown in Figure 8. There were strong and highly statistically significant positive trends across all metrics when using the raw SST data. In contrast, when using the detrended SST data, there were no statistically significant trends (at the 95% confidence interval) across any metric other than the number of events. For the detrended SST data, the maximum intensity trend was only statistically significant at the 90% confidence interval and less than half the trend obtained when using the raw SST data. Furthermore, the trend identified in the number of detrended MHW events is small, at 0.02 events/year, three times smaller than the 0.06 events/year found for the raw SST data.

Figure 8 includes all MHW events detected across the study period rather than just the most severe events shown in Figure 7 and Table 1. This more clearly illustrates the effect of detrending the SST distribution across all metrics values earlier in the study period: their annual averages increase when using the detrended data, whilst average values for the later years typically decline after the detrending process. This effectively removes the significance of the trend in most cases.

3.5. Drivers of MHWs: A Traditional Approach

3.5.1. Case Study: The 2003 Event

Accurate MHW detection leads to MHW events with well-defined start and end dates. This allows for the calculation of MHW metrics across the duration of individual events. The mean intensity and number of MHW days for the extreme 2003 event, calculated using detrended SSTs, are presented in Figure 9, alongside the evolution of anomalies in humidity gradient, heat flux and wind speed. These results are explored in detail below.

The 2003 event was the longest event detected over the course of the study period, lasting 94 days. MHW onset occurred in the WMED, which experienced the greatest mean intensities. While the MHW event reached almost the entire Basin, a large vertical stretch of the CMED remained relatively untouched. The number of MHW days was the greatest in the southern parts of the WMED and CMED, with many locations experiencing over 60 days of MHW conditions. In contrast, the number of MHW days was relatively low in the WMED, indicating that the presence of the event there was intense but short-lived.

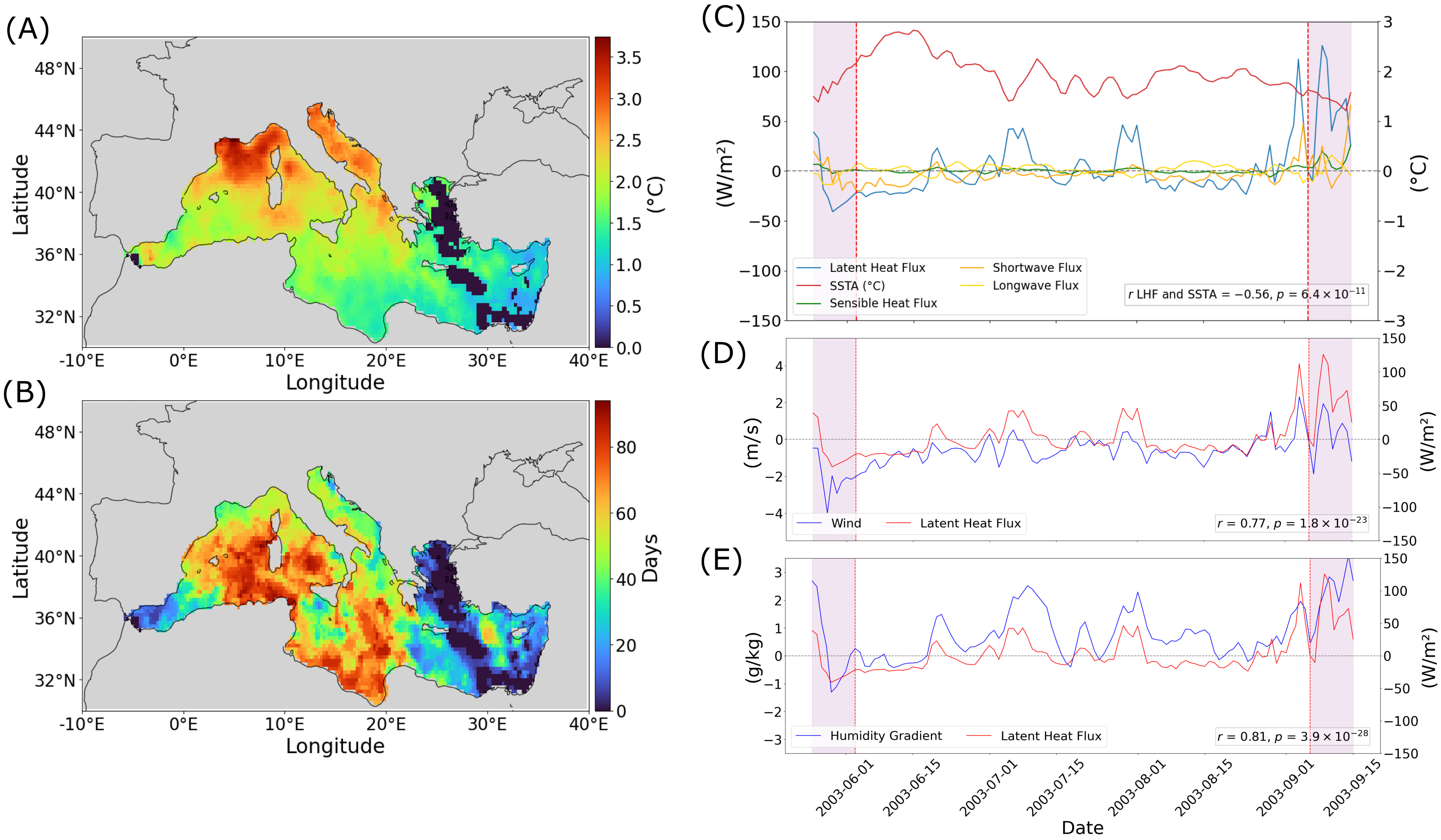

Figure 9. Statistics for the 2003 MHW event, detected using the detrended OISST data. Mean intensity (**A**) and total number of MHW days (**B**) are presented alongside time series of anomalies in air–sea heat flux and SST (SSTA) (**C**), wind speed (**D**) and humidity gradient (q_grad) (**E**). Red dotted lines on the time-series plots indicate the start and end dates of the MHW event. The purple shading indicates the periods 10 days before the start date and 10 days after the end date of the event.

LHF was by far the most variable component of the air–sea heat flux budget during the event, and the correlation between LHF and SST anomalies was significant but moderate, suggesting a relationship between them. Shortly before MHW onset, LHF anomalies became strongly negative and SST anomalies began to rise. In contrast, towards the end of the event, LHF anomalies rose significantly, potentially contributing to an observed drop in SST anomalies. The average climatological value of LHF was around 100 W/m^2 for this period, which means that the positive LHF anomaly peaks describe raw values almost twice as large as their climatology, although the effect is brief and mainly occurs after the event ends and therefore over an area smaller than 15% of the Mediterranean Basin. Shortwave radiation was also significant and presented negative anomalies during the onset of the event. There is also a slight peak in shortwave radiation at the end of the event, although the size of both signals is around half the size of the concurrent LHF anomalies.

Wind speed anomalies were negative leading up to event onset, around 50% lower than their climatological average. Wind speed anomalies remained mostly negative throughout the event, with the occasional peak to positive values during concurrent peaks in LHF anomalies. Immediately before the end of the event, wind speed anomalies became positive and experienced sequential peaks which occurred simultaneously to the peaks in SST. Wind speed anomalies were strongly correlated with LHF anomalies over the duration of the event, with a correlation coefficient of $r = -0.77$. A similar pattern can be seen for the humidity gradient. Humidity gradient anomalies declined before the event to values around 20% lower than their climatological average. Towards the end of the event and the 10-day period afterwards, humidity gradient anomalies rose and were sustained at high values, approximately 50% greater than average. The humidity gradient anomalies were strongly correlated with LHF anomalies during the event, with a correlation coefficient of $r = 0.81$.

3.5.2. Aggregating Across All Events

Figure 10 shows composite anomalies of area-averaged atmospheric variables before and after MHW events, aggregated across all events detected using the detrended SST data. Air–sea heat flux anomalies are dominated by LHF, which on average declines to -25 W/m^2 prior to the onset of an event, and these values are sustained for at least five days after event onset. Anomalies in sensible and longwave heat flux are far less variable than the latent and shortwave terms and are negligible in comparison. Shortwave radiation anomalies vary around -5 $W/m^{\ 2}$ before an event and on average begin to decline 5–10 days prior to the start of an event. Five days prior to the end of an event, LHF anomalies begin to rise rapidly and eventually reach a peak at around 18 W/m^2, although the effect is transient and anomalies quickly decline.

Wind speed anomalies were, on average, negative before an event. The overall shape of the pattern is a slight decline which begins 20 days before an event. Five days prior to the end of an event, wind speed anomalies rise slightly but remain negative and begin a gradual decline as soon as the event ends. Humidity gradient anomalies are relatively insignificant before an event, remaining slightly positive and experiencing a small decline prior to event onset. In contrast, as an event ends, humidity gradient anomalies rise sharply and are sustained at similarly high values for 20 days after the end of the event.

Comparison between composite anomalies and composite values of the reference climatology provides information on the size of the observed anomalies relative to normal atmospheric conditions. The humidity gradient reference climatology averaged around 4–5 g/kg both in the days leading up to an event and the days following an event, which means that the humidity gradient anomalies after the event represent values 10–20% greater than average. Wind speeds averaged at 4.8 m/s before an event and 4.9 m/s after an event, which means that the wind speed anomalies represent wind speeds around 20–25% lower than average before an event and between 10 and 20% lower than average in the days after an event. Finally, LHF averaged at around 80 W/m^2 before an event and 85 W/m^2 after an event. Thus the anomalies presented in Figure 10 represent values 25–30% lower than average before an event, with a brief peak at values 20–25% higher than average following an event.

The same statistics for the 2003 event were calculated across all events. Across the 36 events, LHF anomalies were significantly correlated with SST anomalies for 21 events, with an average correlation coefficient of $r = -0.41$ across all events and an average correlation coefficient of $r = -0.60$ for just the subset of events that had a significant correlation. A linear regression was also performed for each event and was significant for 21 of them, with an average R^2 value of 0.24 across all events and an average R^2 value of 0.37 across events for which the regression was significant. Wind speed anomalies were significantly correlated with LHF anomalies across all 36 events, with an average correlation coefficient of $r = 0.74$. Regressions were significant across all events, with an average R^2 value of 0.57. Humidity gradient anomalies were correlated with LHF anomalies across 35 of the 36 events, with an average correlation coefficient of $r = 0.72$ for all events and $r = 0.74$ across events for which the correlation was significant. Linear regressions were significant across 35 of the 36 events, with an average R^2 value of 0.54 across all events, and 0.55 for events for which the regression was significant.

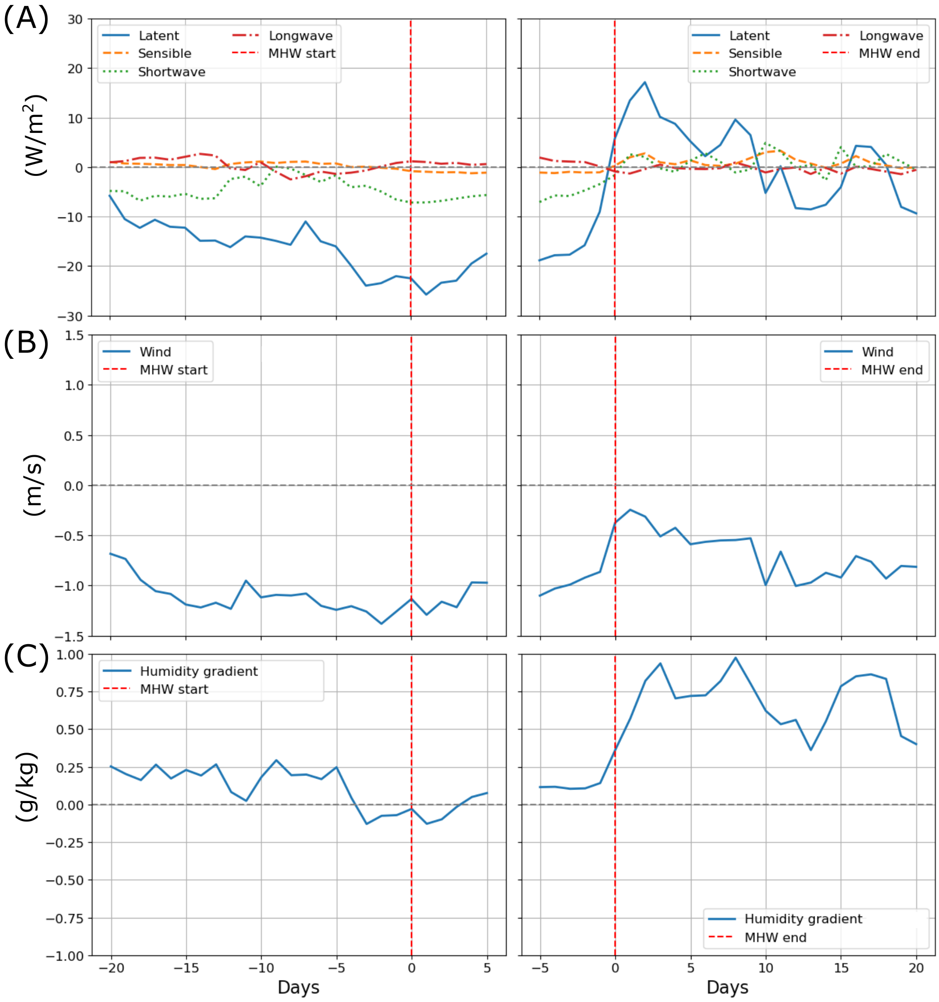

Figure 10. Composite anomalies of air–sea heat flux (**A**), wind speed (**B**) and humidity gradient (**C**). Time values are relative to event start (left panels) and end (right panels). Composites are created by aligning time values across all events.

3.6. EOF Analysis

3.6.1. Major Patterns of Variability

The signals presented in Section 3.5.2 are relatively weak, and wind speed anomalies are about as negative after an event as they are before an event, despite the increased LHF signals after an event, which imply strong changes in either the humidity gradient or wind speed. This indicates that this may not be an appropriate method of analysing atmospheric patterns during an MHW event. EOF analysis is introduced here as an alternative method of analysing interactions between air–sea heat flux and MHWs.

EOF analysis revealed two clear modes of MHW intensity over the course of the study period. The first mode accounted for approximately 31% of the variance in MHW intensity whereas the second mode accounted for approximately 12% of the variance. No other mode accounted for over 5% of the variance. The spatial patterns of the two modes and the evolution of their strength over the study period are shown in Figure 11.

The first mode is positive over almost the entire Mediterranean Basin, with the strongest signal in the northern parts of the WMED and around the coast of Italy, France, and the Adriatic Sea. Just as there was a clear northwest–southeast gradient in MHW intensity in Figure 9, there is also a northwest–southeast gradient in the EOF pattern of mode 1. The strength of the mode decreases moving southwards and declines to near zero in the Aegean Sea and EMED. The normalised PC time series of both modes look somewhat discontinuous, as only MHW intensities over the study period (31 May–26 September) are shown, leading to stretches of 0 score between years. The time series of PC1 is the strongest in 2003, in line with the major 2003 event, but is also strong in 1987, 1994, 1998, 2015, and 2023. This is concurrent to some of the most extreme MHW events, as established in Table 1.

In contrast to mode 1, the spatial pattern of mode 2 presents a dipole pattern, with positive MHW intensities concentrated within the Gulf of Lions and throughout much of the WMED, decreasing towards the Strait of Gibraltar and the east coast of Sardinia. Throughout the CMED and the Adriatic Sea, the signal of mode 2 is strongly negative over large areas. Unlike mode 1, there is a signal present in the Aegean Sea, which is negative. The intensity of the signal then declines moving towards the Levantine Sea. The PC time series of mode 2 has both positive and negative scores. A strong mode 2 signal is present in the years 1998, 2003, 2018 and 2022–2024 (negative) and in the years 2003, 2018 and 2022 (positive).

3.6.2. Drivers of Principal Component Events

Figure 12 illustrates the behaviour of key atmospheric and oceanic variables before and after the onset of a PC MHW event. These were defined following the methodology presented in Section 2.7. PC1 (mode 1) and PC2+ (mode 2) events correspond to the results of performing this alternative detection method with a 90% normalised score threshold for each PC, whereas PC2− (mode 2) events correspond to events which are defined relative to the PC time series falling below its 10th percentile threshold. Altogether 22 events were detected for PC1 and PC2+, and 16 events were detected for PC2− (Tables A1–A3). To test the sensitivity of the PC MHW event definition, events were also detected using a 5-day rather than 10-day minimum duration. This yielded a total of 119 PC MHW events, and composite anomalies of atmospheric variables over their duration are shown in Figure A2.

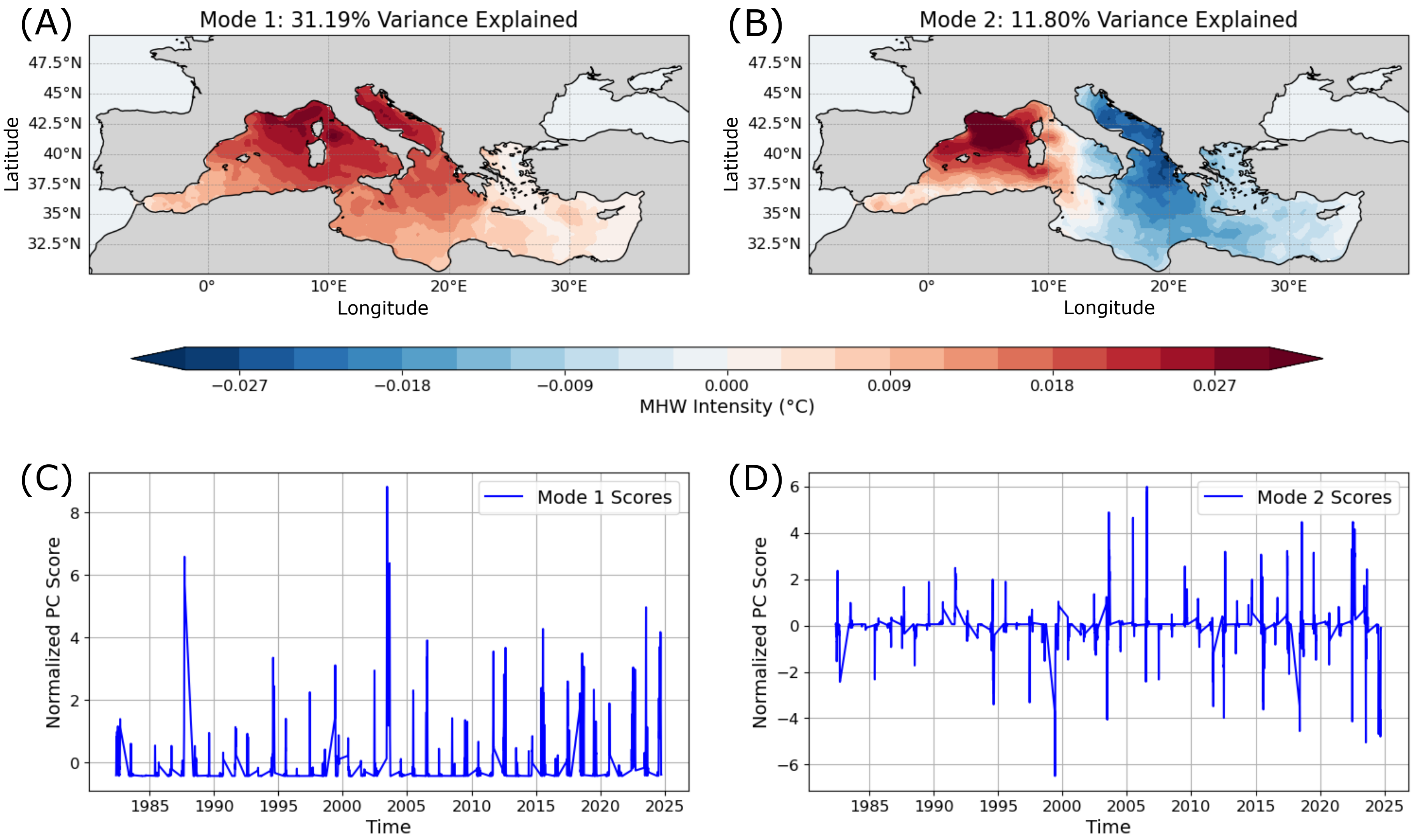

Figure 11. Spatial patterns (empirical orthogonal functions) of the two dominant modes of variability in MHW intensity (**A**,**B**). The normalised time series (**C**,**D**) of the associated principal components (PCs) are presented below. These patterns were retrieved from EOF analysis of MHW intensities between 31 May and 26 September over the 1982–2024 period.

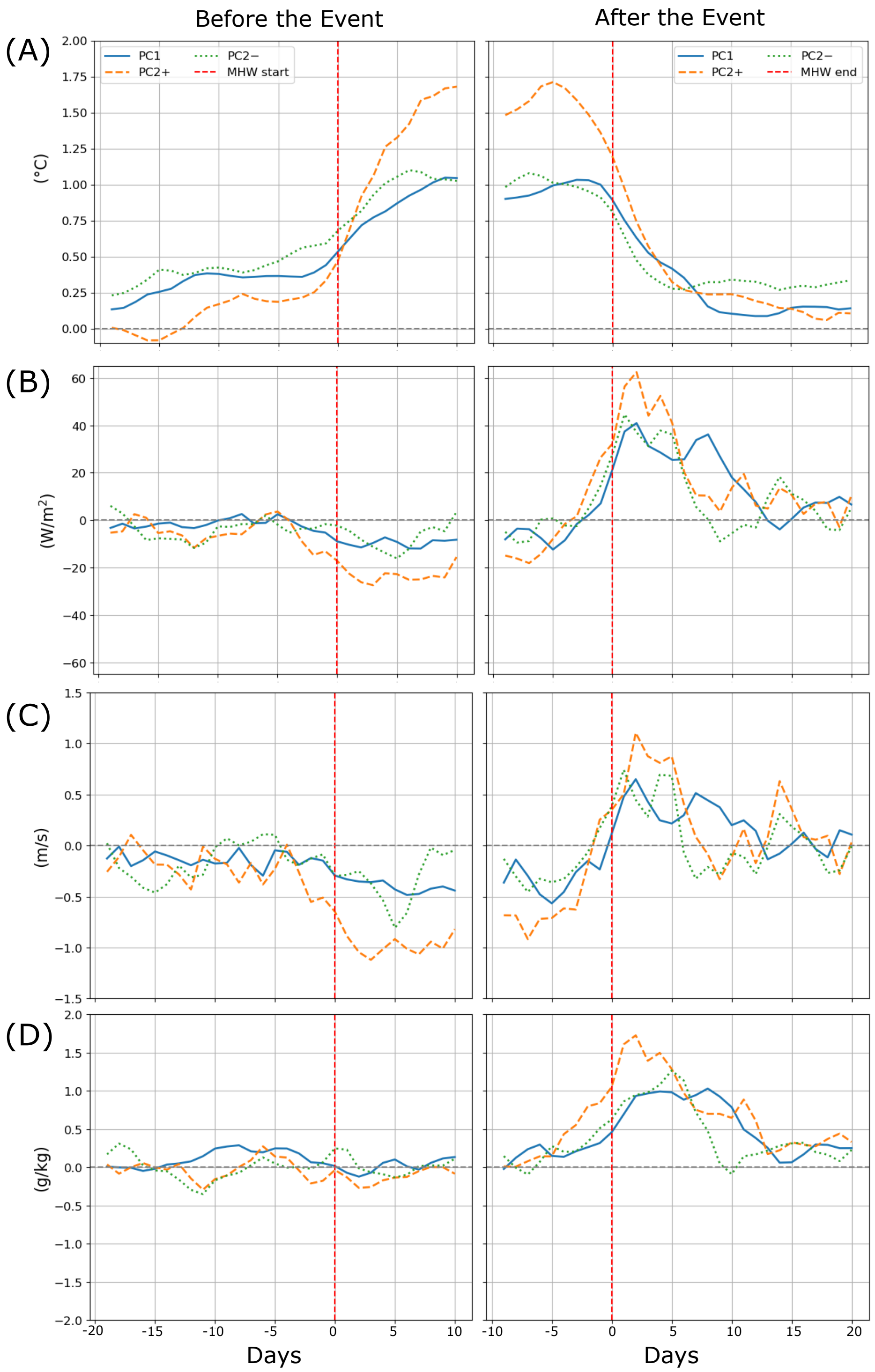

Figure 12. Composite time series of (**A**) SST, (**B**) LHF, (**C**) wind speed and (**D**) humidity gradient anomalies before and after the three different kinds of PC MHW events. PC1 refers to the first PC, and PC2+ and PC2− refer to the positive and negative phases of the second PC, respectively. A PC MHW occurs when a PC exceeds the 90th percentile of its climatology in its positive phase or drops below the 10th percentile of its climatology in its negative phase, for 10 days or more. For PC1, anomalies are averaged over the whole Mediterranean from −5° to 35° E. For PC2+, anomalies are averaged between 37.5–44° N and 0–10° E. For PC2−, anomalies are averaged over 32–45° N and 15–35° E. Red dotted lines mark PC MHW events' start and end dates. Time values are relative to an event's start (**left panels**) and end (**right panels**). Composites are created by aligning time values across all events.

For all components, detrended SST anomalies remain relatively stable until around 5 days prior to the start of an event, before rapidly increasing. SST anomalies for PC2+ events demonstrate the strongest increase, to around 1.5 °C, while anomalies for PC1 and PC2− events increase to around 1 °C. PC2+ SST anomalies begin to decline 5 days prior to the end of an event, whereas anomalies for PC1 and PC2− events decline later and simultaneously to the end of their respective events. LHF anomalies before a PC event are small until the 5 days prior to an event's start, when for all PC events, LHF anomalies start to become more negative. This is strongest for PC2+ events, with decreases of around half the size experienced by PC1 and PC2− events. In contrast, LHF anomalies are much more appreciable after an event, rising rapidly for all PCs 5 days prior to the end of an event. The effect is once again the largest for PC2+ events, although sizeable peaks are seen in both PC2− and PC1 events. For PC1 events, these anomalies are sustained for the longest time and persist until around 10 days after the end of a PC MHW. A similar pattern presents itself for wind speed anomalies, which are strongly negative before an event for PC2+ events. For PC2− and PC1 event anomalies are negative but only reach values of around half the size of their PC2+ counterpart. Five days prior to an event's end, wind speed anomalies rise to strong positive values for all PC events, with once again the largest peak being experienced by PC2+, and anomalies were sustained for the longest time for PC1 events.

Across all kinds of PC events, there is no clear pattern in humidity gradient anomalies before an event, although the pattern after an event is much clearer. Ten days before the end of a PC event, humidity gradient anomalies begin to increase steadily, with the strongest peak for PC2+ events. Unlike the pattern for wind speed and LHF anomalies, the temporally integrated humidity gradient anomalies are the largest for PC2+ events, although the value is still large for PC1 events.

3.6.3. Spatial Patterns

Spatial maps of LHF, wind speed and humidity gradient anomalies, averaged over the 5 days following a PC event, are shown in Figure 13. For LHF anomalies, the map for PC1 events shows negative anomalies spread across the WMED, CMED and Adriatic Sea, with slight positive anomalies in the EMED and southern CMED. PC2+ events experience negative LHF anomalies over a smaller area, primarily in the WMED. For PC2+ events, positive anomalies are seen across the Adriatic Sea, the CMED and parts of the EMED, with weak negative anomalies in the WMED. PC2− events have some of the most strongly negative LHF anomalies, which are experienced in a relatively small region in the Gulf of Lions. Elsewhere, anomalies remain negative, except over the Aegean Sea, where anomalies are strongly positive.

In most cases, wind speed anomalies follow a similar pattern to LHF, although the signal is patchier in some regions. In particular, the pattern for PC2+ events is much less consistent for wind speed than for LHF anomalies. This is particularly apparent in the CMED, where wind values are generally weak and alternate between regions of negative and positive anomalies. Wind anomalies most closely align with LHF anomalies for PC2− events, where they are the weakest in the WMED and CMED. Very strong positive anomalies can be seen in the Aegean Sea.

As with the more traditional detection method, humidity gradient anomalies are relatively weak before an event. For PC1, negative anomalies are concentrated in the WMED and Adriatic Sea, with positive anomalies over the southernmost parts of the CMED, as well as the EMED. For PC2+, anomalies are mostly positive, and for PC2−, weak negative anomalies encompass the WMED, CMED and Adriatic Sea, with weak positive anomalies across the EMED.

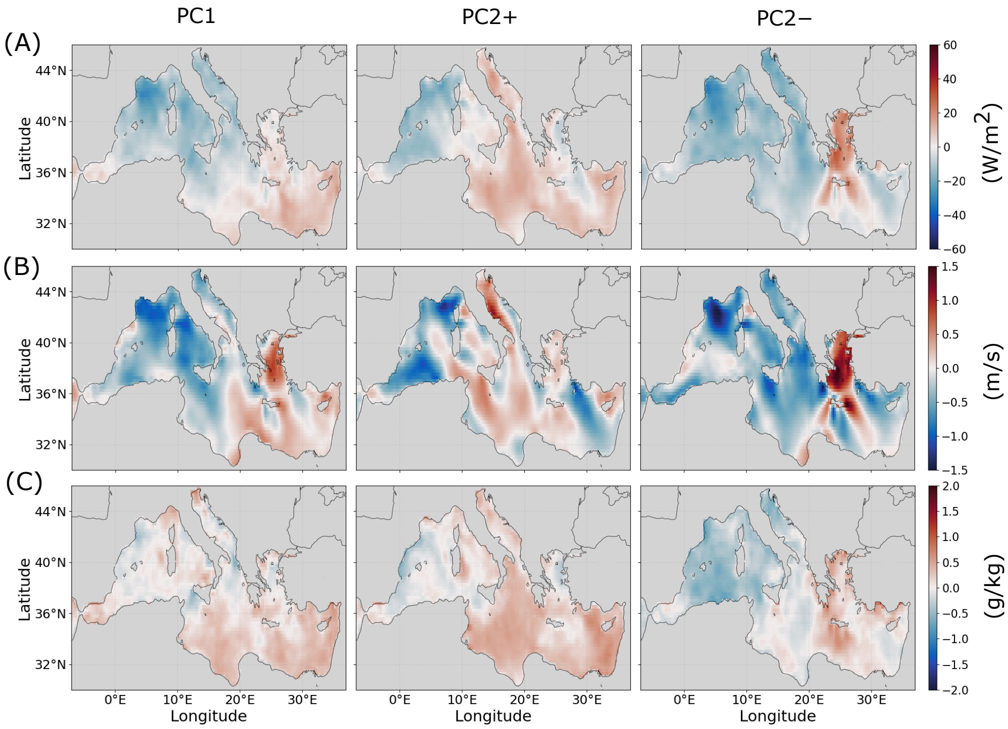

Figure 13. Composite anomalies of LHF (**A**), wind speed (**B**) and humidity gradient (**C**) averaged over the 5 days immediately preceding PC1, PC2+ and PC2− MHW events.

LHF, wind and humidity gradient anomalies averaged 5 days after an event are shown in Figure 14. LHF anomalies are strongly positive for PC1 events over almost the whole Basin, with anomalies being the strongest in the WMED and declining on an eastward gradient towards the EMED. LHF anomalies are similarly strongly positive for the WMED for PC2+ events. For PC2− events, the clear WMED signal has disappeared, replaced by strong LHF anomalies in the CMED and EMED, with negative anomalies in a small region within the Gulf of Lions. Across all PC events, the largest anomaly values after the event were almost thrice as large as for the greatest values before an event, covering and being sustained over a much wider area.

A similar pattern occurs for wind anomalies, with strong positive anomalies in the WMED for PC1 and PC2+ events. PC2− events have the strongest wind anomalies in the CMED and EMED and have weak negative or positive anomalies in the WMED. Wind speed anomalies are much stronger after an event than before an event, and they cover larger regions.

Humidity gradient anomalies are positive everywhere for both PC1 and PC2− events, with PC1 events showing almost double the magnitude of the values before a PC1 event. These strong positive anomalies extend over the entire WMED and Adriatic Sea, declining on an eastward gradient towards the EMED. For PC2+, humidity gradient anomalies reach similar strengths over the WMED, but weak negative anomalies can be seen over the EMED. For PC2− events, anomalies are similarly strong, particularly in the Adriatic Sea. Humidity gradient anomalies after an event are more consistent with the expected relationship between humidity gradient and LHF than before the event, with the spatial patterns following one another closely.

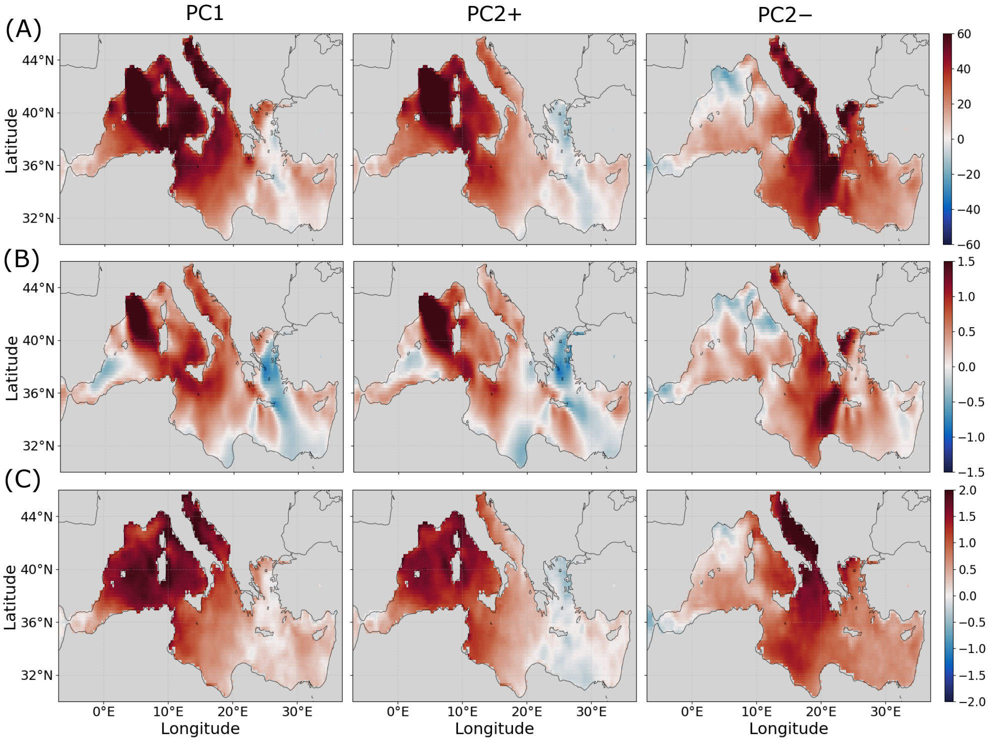

Figure 14. Composite anomalies of LHF (**A**), wind speed (**B**) and humidity gradient (**C**) averaged over the 5 days immediately after PC1, PC2+ and PC2− MHW events.

4. Discussion

The aim of this study was to catalogue extreme MHWs in the Mediterranean Sea and to use this catalogue to determine how air–sea interactions influence the evolution, onset and decline of Mediterranean MHWs. Addressing these aims required a number of preliminary steps, as well as the introduction of an alternative methodology. The results of the study are discussed within the context of these aims below.

Section 3.1 found strong positive SST trends throughout all Mediterranean sub-basins. These results were verified by using the same method to calculate annual trends (Figure A1), which agree within uncertainty bounds with trends calculated between 1979 and 2024 using the same dataset [39]. The strong positive SST trends demonstrate the importance of detrending SSTs before MHW detection, since SST trends are the dominant driver of MHW trends [22]. If a fixed climatology were used, the MHWs occurring later in the study period would appear more intense and last longer than the MHWs which occurred earlier, even if the contribution of short-term variability to their SST values were the same. The anomaly distributions presented in Section 3.2 illustrate this further. Before detrending, the mean of the SST anomaly distribution varies by up to 0.8 °C between the 1982–2002 and 2003–2024 periods. This would lead to overestimates of MHW intensity during the later period and underestimates of MHW intensity during the earlier period. The process of detrending restores the means of both distributions to almost 0 °C, removing as much of this bias as possible. The resulting distributions of SST anomalies are very similar to the distributions produced by Martinez et al. [26], despite small differences in study period and methodology.

The maps presented in Figure 6 illustrate the effect that the detrending process has on MHW detection in the Mediterranean Basin. Spatial patterns agree well with the literature for the raw values, reproducing the expected northwest–southeast gradient in mean, maximum and cumulative intensity [1,40,41]. The count of total MHW days is the greatest in the southern EMED, northern CMED, eastern WMED and Adriatic Sea, following the pattern reported by [41]. For mean and cumulative intensity, as well as total MHW days, the detrended SST data show decreases across all metrics in most regions. The EMED typically experienced the greatest decrease in MHW days of any region, which is supported by Pastor and Khodiyar [20], who identified the strongest trends in MHW days in the eastern Levantine Sea. Cumulative intensity correspondingly declines the most in the EMED, since this metric depends strongly on MHW days. Despite having strong SST trends, the WMED has the weakest trends in MHW duration [41], which explains why MHW days in this region experience relatively little decline.

Performing MHW detection on detrended SST data yields an event catalogue which identifies the 2003 event as the most severe over the study period, consistent with Martinez et al. [26]. The 2003 event is well-known as a particularly impactful event, and concurrent mass mortality events within benthic ecosystems have been widely reported [42]. In contrast, the 2024 event experiences a large decrease in severity—extreme SST anomalies during this event are more a product of the background warming trend than a reflection of short-term variability. However, the impacts from such events must not be minimised. The 2024 event has been linked to the intense flowering of *Posidonia Oceanica* meadows within the Adriatic Sea [43], potentially having a severe impact on their resilience. This was the product of the total thermal stress the organism was placed under, which, for organisms which do not have the capacity to rapidly adapt, is more directly linked to raw rather than detrended temperature thresholds. Therefore the detrended and raw catalogues of MHW events should be viewed as complementary, with the choice between the two depending on the specific research question: raw SSTs better reflect ecological impacts, whereas detrended SSTs better represent the short-term dynamics of the physical climate.

No statistically significant trends were found across all metrics except the frequency of events for the annual averages of the detrended event catalogue. This is consistent with recent findings that the background warming trend is largely responsible for observed trends in MHW metrics [22,23]. However, by the same reasoning, we would not expect a significant trend in event frequency, which we find in Figure 8, which disagrees with Martinez et al. [26]. A possible explanation is that later MHW events are more often split into separate events as an effect of the stricter temperature threshold imposed by detrending. For example, the two 2022 events in the raw data are split over three events in the detrended data.

The definition of an MHW with a minimum spatial extent is intended to isolate the most extreme MHWs whilst ignoring local events with small or negligible impacts [20]. However, varying choices as to the spatial extent which is considered “extreme” makes comparison between studies difficult, as can be seen with the difference between the raw events catalogued here and those in [29]. A further challenge is presented by the fact that the minimum spatial extent is defined to be non-contiguous. This issue is particularly important when considering that the objectives of this study are to assess physical drivers of MHW events. The atmospheric patterns experienced by disconnected MHW grid points on opposite sides of the Mediterranean may vary drastically, but both groups are counted as part of the same event. A more robust definition would therefore define a single event as a region of connected points. This approach has recently gained traction, and a number of studies on spatially continuous MHWs (SCMHWs) have been performed in recent years (see [44,45]).

The analysis of the 2003 event presented in Section 3.5.1 provides the first opportunity for analysing the influence of atmospheric drivers on MHW evolution. While the event affected almost the entirety of the Mediterranean, the Aegean Sea was relatively unaffected. In Section 3.6 we see that the two significant modes of MHW intensity are preceded by strong winds over the Aegean Sea before they reach their strongest values. The 2003 event overlaps with multiple PC MHWs (Tables A1–A3) so the relatively low activity over the Aegean may be a direct representation of this pattern. While the majority of the Mediterranean experiences reduced wind speeds, higher-than-average wind speeds in the Aegean Sea may prevent the event from spreading there. A strong LHF anomaly is found both before and after the 2003 event, with LHF reaching peaks of 100 W/m^2 or more after an event, i.e., over five times the average value when the same analysis is aggregated over all events in Section 3.5.2. The timing of this peak suggests that the LHF anomaly is the product of heat release from the MHW during its decay. Wind is strongly correlated with LHF over the 2003 event, suggesting that it plays a role in its evolution, as expected from Equation (3). In contrast, humidity gradient anomalies show a more transient decline immediately before an event, which may suggest that it had more limited influence on the onset of the 2003 event. These results are consistent with similar findings of reduced wind speeds across the Mediterranean during the 2003 MHW event [46].

Section 3.5.2 aggregates these results across all events, finding that LHF is by far the biggest term of the air–sea heat flux budget during an MHW event. Figure 10 establishes a link between decreased wind speed and MHW onset, with positive humidity gradient anomalies linked to increased LHF anomalies after an event. One of the most surprising features of Figure 10 is that wind speed anomalies on average never reach positive values following an event, and their values are almost as negative as the anomalies preceding an event. This is unexpected, since decreased winds are often associated with the onset of an MHW event, but a similar signal is not generally seen after an event [47].

One reason for these signals may be due to the difficulty in isolating clear onset and decay phases over multiple events. Since the maximum permissible gap between two separate events is 2 days, the periods before and after the start and end dates of multiple events can easily overlap. Furthermore, 15 of the identified MHW events lasted fewer than 10 days, likely having shorter-lasting atmospheric interactions than major events such as the 2003 event, so the reliability of the time series presented in Figure 10 decreases with the increase in the time that has passed between a given value and an MHW start or end date. Another issue is that the signals presented in Figure 10 are area-averaged over all MHW grid points for each day. As mentioned previously, disconnected grid points may have different physical drivers, but these grid points are also not necessarily coordinated in their evolution–a group of connected grid points in the WMED may be experiencing event onset due to reduced wind speeds at the same time as a group of grid points in the EMED experiences MHW decay due to increased wind speeds, smoothing out any atmospheric signal we wish to retrieve.

EOF analysis directly addresses these concerns by splitting the signal of MHW variability into fixed spatial patterns. For example, PC2+ results are area-averaged over an interconnected region of the WMED, all of which experiences the same pattern of high intensities during a PC2+ event. Since the region consists of points closer together, they are likelier to experience the same atmospheric conditions. On top of this, the evolution of the grouped points may be more synchronised. This is because the intensity of each spatial pattern is controlled by a single time series. Grid points in the PC2+ region therefore become more or less intense at roughly the same times. Furthermore, rather than one composite time series for all events, by splitting MHW variability into three patterns, the spatial characteristics of MHW drivers are better preserved. For example, PC2+ describes atmospheric conditions which promote MHW activity over solely the WMED, while PC2− investigates the conditions which lead to MHW events in the Adriatic, CMED and EMED. Overall EOF analysis constructs a more robust synthesis of MHW drivers across multiple events.

Simon et al. [48] performed EOF analysis on MHW activity, which is the product of spatial extent, mean intensity and duration. This is similar to event severity as defined here, except activity is calculated for individual grid points. They found a positive pattern everywhere for their first PC, with the greatest values in the WMED, similar to the pattern for PC1 in Figure 11. Their second PC also showed a distinct dipole pattern between the WMED and the rest of the Basin, in agreement with PC2 presented here. Further comparison can be made between the results presented here and the application of the same method to the Indian Ocean by Joseph et al. [38]. In their atmospheric time series, they also found negative LHF anomalies prior to MHW start, although shortwave radiation, which does not contribute significantly for the Mediterranean case, was also found to play a significant role. This is likely due to the Indian Ocean having relatively greater cloud cover than the Mediterranean, particularly during the monsoon season, over which their study was conducted [49]. The Indian Ocean study also found reduced wind speeds of a similar magnitude before an event, consistent with the observations here.

The advantages of the EOF approach can be seen in Figure 12, where stronger signals are found across all variables for the PC1, PC2+ and PC2− events than when they are defined more traditionally (Figure 10). The LHF signal after a PC event is over double that of the signal seen with the traditional approach. Before an event, composite anomalies of LHF for PC2+ are roughly twice as large as LHF anomalies for PC1 and PC2−, which may contribute to the fact that SST anomalies are around 50% higher during PC2+ events. This is consistent with the work of Section 3.3, as well as the literature, with both reporting the greatest MHW intensities in the WMED and particularly over the region where PC2+ is the strongest [1]. By separating patterns in MHW intensity into orthogonal components which impact different regions, an explanation is suggested for this pattern—LHF anomalies are unusually negative before the strongest episodes of MHW activity occur in this region, concurrently with negative wind anomalies almost twice as strong as the signals for PC1 and PC2−. The count of total MHW days is also the largest in this region, and not only are LHF anomalies the most negative for PC2+ events before an event, but they are also sustained at these values for longer than both PC1 and PC2− events. This may explain why this region experiences some of the highest counts of total MHW days (Figure 9).

One aspect which is consistent across both the traditional and EOF approaches is that MHWs are preceded by negative wind speed anomalies. Bonino et al. [28] associate the negative wind speed anomalies which precede a Mediterranean MHW with the formation of long-lasting subtropical ridges. In the Mediterranean, subtropical ridges represent the northerly expansion of the subtropical high-pressure belt, and the weakened winds which follow were demonstrated to be the main driver of MHW onset. Bonino et al. [28] also note that these high-pressure intrusions alternate with regions of low pressure. The propagation of these features as part of a wave-train across the Mediterranean could be a potential explanation for the positive wind anomalies seen after an event, although this remains speculative without further analysis.

By presenting a potentially more robust methodology, the EOF approach provides further insights into some of the questions presented by the results of the traditional approach in Section 3.5.2. In Section 3.5.2, wind anomalies were negative before an event but remained about as negative even after an event, contrary to both reports in the literature [47] and the pattern expected by Equation (3). The opposite pattern is presented by the results of the EOF approach in Figure 12, with wind anomalies being strongly positive after a PC event. This suggests that the reason for the negative anomalies presented in Figure 10 is the result of the method smoothing out the true signal. However, neither the EOF nor the traditional approach finds an appreciable signal in humidity gradient anomalies preceding an event, implying that the humidity gradient contributes little to the decline in LHF which precedes an event.

Further detail can be seen in the spatial patterns of atmospheric variables before a PC MHW, as presented in Figure 13. Atmospheric signals in most cases follow the spatial patterns presented in Figure 11, with decreased LHF and wind speed anomalies in regions of positive MHW intensity and relatively weak or positive anomalies in regions with weak or negative MHW intensity for each PC. An exception is the Aegean Sea, which is mainly subject to PC2− events, with concurrent strong wind and LHF patterns seen before an event rather than after. This pattern may indicate that a mechanism other than LHF drives MHW activity in the Aegean Sea, which has been linked to the advection of Black Sea water [50] and changes in the East Atlantic/West Russia pattern [51].

Another pattern unique to the EOF analysis is that LHF anomalies after an event are roughly two–three times greater than LHF anomalies before an event. For the traditional approach, the peaks in LHF were roughly the same before and after an event. Figure 12 suggests that this is due to the fact that before an event, negative LHF anomalies are impacted by weakened winds, whereas after an event, positive LHF anomalies are associated with the compound effect of both strong winds and a strong humidity gradient. An extension of this work could be to analyse the drivers of saturation and specific humidity across a wider range of atmospheric variables. This could establish why humidity gradient anomalies are strong after but not before an event, identifying the cause of this asymmetric pattern.

While the EOF approach holds significant advantages over the more traditional approach outlined in Section 2.5, it also presents several drawbacks. One issue is that the technique has rarely been applied to investigate links between MHW activity and atmospheric variables, so the definition of what defines a “PC MHW event” remains subjective. It is not necessarily the case that defining a 90% threshold for each PC signal isolates MHW activity of comparable extremity to the traditional approach. In fact, the smaller number of events in Tables A1–A3 suggests that this definition is actually too strict. The stronger signals presented by Figure 12 may thus be partly due to a harsher detection criterion rather than an improved methodology, with more severe events naturally presenting stronger atmospheric signals. However, it should also be noted that many PC events also have no concurrent MHW event. The choice of PC MHW definition must therefore balance consistency with known MHW events and the misidentification of low-impact events as extremes. Weakening the detection criterion from a 10-day to a 5-day threshold yields an additional 59 PC MHW events, and the associated atmospheric patterns are shown in Figure A2. As we would expect from considering less extreme events, anomalies generally decrease in magnitude, yet the overall patterns remain the same as in Figure 12. In particular, wind anomalies remain positive rather than negative after an event, and there are still stronger LHF signals than the traditional approach detects in Figure 10.

On top of this, while we identify LHF as the dominant air–sea heat flux interacting with MHW events, a full heat budget analysis is necessary to assess the impacts of its heating and cooling contributions relative to other drivers, such as the advection of heat and vertical mixing. There is consequently some uncertainty left as to how significant the contribution of LHF is to the total gain and loss of heat by the ocean. However, we are investigating only the most extreme events, defined principally by their extent. The dominant drivers of MHWs are very sensitive to spatial scale. Results from a global heat budget analysis suggest that the Mediterranean transitions between the ocean-driven and atmosphere-driven MHW regimes exist on spatial scales between $0.1^\circ \times 0.1^\circ$ and $2^\circ \times 2^\circ$ [52]. The 15% spatial threshold used by this study and the large regions which define each PC event mean that the typically considered MHW events exceed this scale. The relatively small transition scale is consistent with the fact that that the Mediterranean is semi-enclosed, so we may expect that SSTs are forced more by atmospheric interactions than ocean processes. This is also supported by a separate heat budget analysis which attributes the majority of the

SST change during large-scale MHW onset to heat flux forcing throughout most regions of the Mediterranean [28]. While it is therefore likely that surface heat fluxes are a very significant contributor to the MHW events studied here, a full heat budget would give a more complete picture and enable a more detailed interpretation of MHW events on a regional scale.

5. Conclusions

A detrended approach to MHW detection correctly restores the idea of an MHW event as a statistical extreme. However, while a detrended approach with a minimum spatial extent was found to be well-motivated within the context of the universal framework set out by Hodbay et al. [19], the results of the composite anomaly analysis in Figure 10 imply that this leads to atmospheric signals being obscured. This prompts the use of EOF analysis, which has been shown to be an effective tool for producing more spatially coherent information about MHW interactions with the atmosphere.

LHF dominates the air–sea heat flux budget of a Mediterranean MHW, with LHF anomalies becoming steadily more negative 5 days prior to an event. In general this decreased evaporation signal can be sustained for 10 or more days. A likely contributor to these anomalies is decreased wind speed, since wind speed anomalies also become strongly negative 5 days prior to the start of an event and are similarly sustained at these values for long periods. The pattern of decreased wind speeds and subsequent decrease in outgoing LHF provides a connection between the physical drivers associated with MHWs and the larger-scale atmospheric circulation, since this pattern has been strongly linked to the increased formation of subtropical ridges [28].

After an event, LHF anomalies were found to be around three times greater in magnitude than before an event. A possible cause of the different atmospheric patterns before and after an MHW event is that after an event, both humidity gradient and wind anomalies become more positive, exerting a compound influence on LHF anomalies. Before an event, there is only an appreciable pattern in wind speed anomalies. This was demonstrated to be the average pattern across all PC MHW events in the Mediterranean over the course of the study period.

A greater understanding of the atmospheric drivers and ocean feedback of MHW events will lead to more precise predictions of their impacts in the future. This is of particular importance for extreme weather events such as medicanes, which have significant potential to be influenced by the interaction between MHW events and the air–sea heat flux budget. The results presented here demonstrate a link between MHWs and distinct evaporation patterns which vary on a sub-regional scale. Future work which accounts for the full MHW heat budget is essential to providing coastal communities with the knowledge they need to adapt to a rapidly changing climate and its compound extremes.

Author Contributions: Conceptualisation, N.S. and C.P.; methodology, N.S., C.P. and L.J.; software, N.S., C.P. and L.J.; validation, N.S. and C.P.; formal analysis, C.P.; investigation, C.P.; resources, C.P.; data curation, C.P.; writing—original draft preparation, C.P.; writing—review and editing, N.S., C.P. and L.J.; visualisation, C.P.; supervision, N.S.; project administration, N.S. All authors have read and agreed to the published version of the manuscript.

Funding: This research study received no external funding. L.J. was supported by the Natural Environment Research Council [Grant NE/S007210/1].

Data Availability Statement: The monthly OISST dataset (version 2) was provided by the PLS NOAA https://psl.noaa.gov/data/gridded/data.noaa.oisst.v2.highres.html) (accessed on 7 May 2025). The daily ECMWF ERA5 reanalysis data were retrieved from the E.U Copernicus Marine

Service (https://cds.climate.copernicus.eu/datasets/derived-era5-single-levels-daily-statistics?tab=overview) (accessed on 12 May 2025).

Acknowledgments: During the preparation of this manuscript, C.P. made limited and mindful use of ChatGPT (OpenAI, GPT-5) for the purposes of writing refinement. The authors have reviewed and edited the output and take full responsibility for the content of this publication.

Conflicts of Interest: The authors declare no conflicts of interest.

Appendix A

Appendix A.1. Annual SST Trends in the Mediterranean

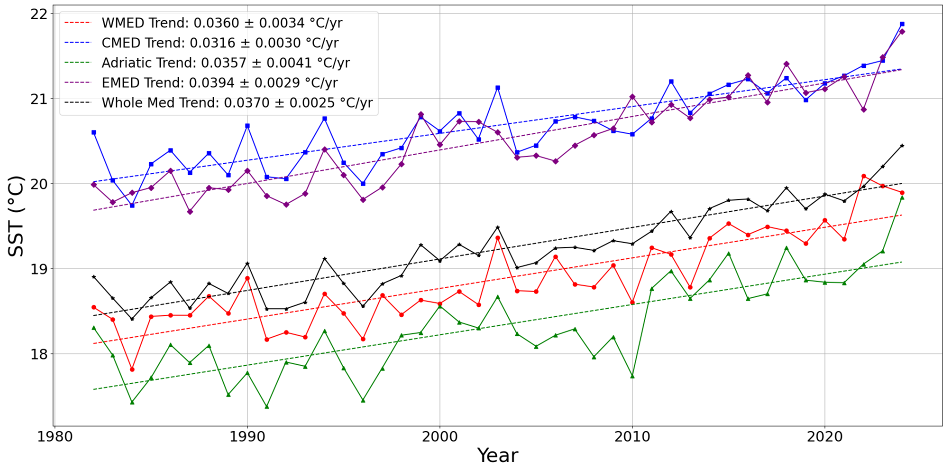

Figure A1. Time series of annually averaged SST values over the whole year from 1982 to 2024. Coloured solid lines show the time series for each sub-region. The linear fits were calculated from all daily data over this period. Trends are split into 4 sub-regions as outlined in Section 2.2.

Appendix A.2. Atmospheric Anomalies for PC MHW Events with a 5-Day Threshold

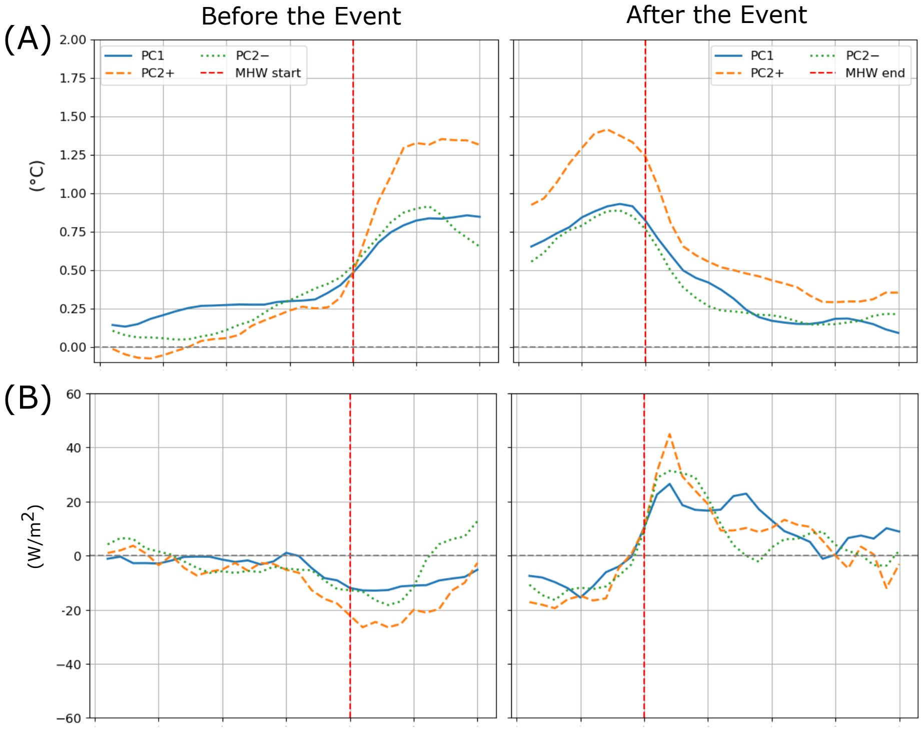

Figure A2. *Cont.*

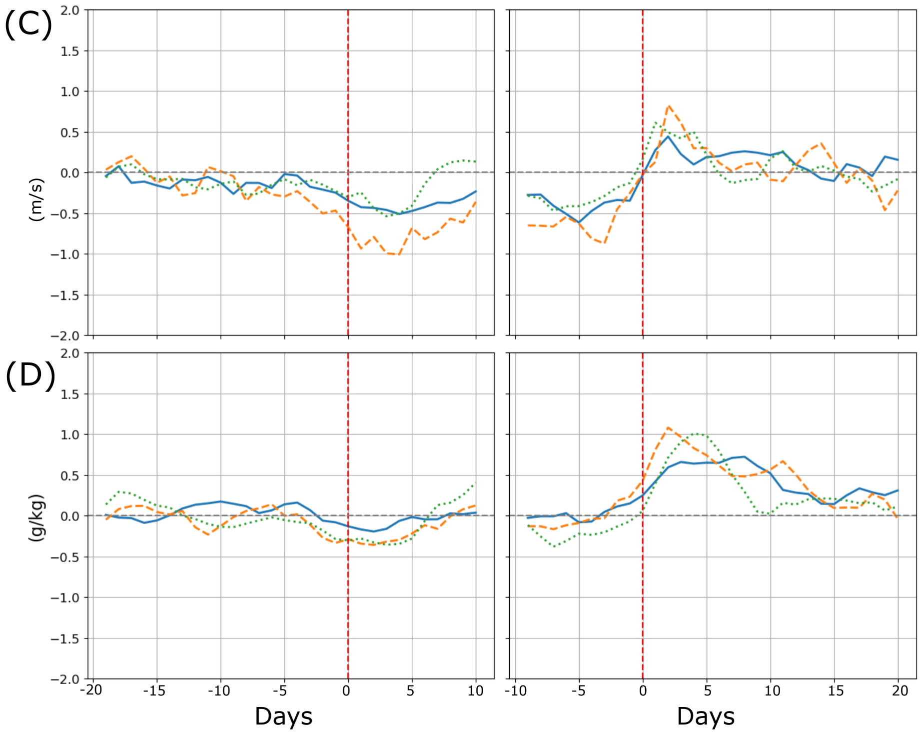

Figure A2. Composite time series of (**A**) SST, (**B**) LHF, (**C**) wind speed and (**D**) humidity gradient anomalies before and after the three different kinds of PC MHW events when detected using a minimum 5-day threshold. Red dotted lines mark PC MHW events' start and end dates. Time values are relative to events' start (**left panels**) and end (**right panels**). Composites are created by aligning time values across all events.

Appendix A.3. PC MHW Events in the Mediterranean in 1982–2024

Table A1. PC1 MHW events detected between 31 May and 26 September over the 1982–2024 period, matched with concurrent MHW events detected with the method of Section 3.4.

PC1 Start	PC1 End	PC1 Days	MHW Start	MHW End	MHW Days
12 Sep 1987	26 Sep 1987	14	10 Sep 1987	26 Sep 1987	16
3 Aug 1994	11 Sep 1994	39	3 Aug 1994	20 Sep 1994	48
31 May 1999	15 Jun 1999	15	31 May 1999	13 Jun 1999	13
31 May 2000	10 Jun 2000	10	–	–	–
16 Jun 2002	25 Jun 2002	9	18 Jun 2002	24 Jun 2002	6
31 May 2003	15 Jul 2003	45	4 Jun 2003	5 Sep 2003	93
24 Jul 2003	6 Sep 2003	44	4 Jun 2003	5 Sep 2003	93
20 Jun 2005	29 Jun 2005	9	20 Jun 2005	28 Jun 2005	8
9 Jul 2006	2 Aug 2006	24	12 Jul 2006	3 Aug 2006	22
7 Sep 2011	19 Sep 2011	12	8 Sep 2011	21 Sep 2011	13
5 Jul 2012	15 Jul 2012	10	1 Jul 2012	16 Jul 2012	15
16 Aug 2012	27 Aug 2012	11	16 Aug 2012	30 Aug 2012	14
15 Jul 2015	8 Aug 2015	24	15 Jul 2015	19 Aug 2015	35
11 Jun 2017	27 Jun 2017	16	11 Jun 2017	27 Jun 2017	16
30 Jul 2018	13 Aug 2018	14	29 Jul 2018	13 Aug 2018	15
11 Sep 2018	24 Sep 2018	13	7 Sep 2018	24 Sep 2018	17
28 Jun 2019	9 Jul 2019	11	30 Jun 2019	8 Jul 2019	8
13 Sep 2020	26 Sep 2020	13	12 Sep 2020	25 Sep 2020	13
16 Jul 2022	17 Aug 2022	32	15 Jul 2022	16 Aug 2022	32
3 Sep 2022	16 Sep 2022	13	2 Sep 2022	17 Sep 2022	15
10 Jul 2023	26 Jul 2023	16	12 Jul 2023	4 Aug 2023	23
8 Aug 2024	12 Sep 2024	35	13 Jul 2024	14 Sep 2024	63

Table A2. PC2+ MHW events detected between 31 May and 26 September over the 1982–2024 period, matched with concurrent MHW events detected with the method of Section 3.4.

PC2+ Start	PC2+ End	PC2+ Days	MHW Start	MHW End	MHW Days
8 Jul 1982	23 Jul 1982	15	–	–	0
11 Aug 1989	24 Aug 1989	13	18 Aug 1989	22 Aug 1989	4
27 Aug 1991	26 Sep 1991	30	4 Sep 1991	24 Sep 1991	20
29 Jul 1995	8 Aug 1995	10	–	–	0
2 Aug 2003	10 Sep 2003	39	4 Jun 2003	5 Sep 2003	93
17 Jun 2005	30 Jun 2005	13	20 Jun 2005	28 Jun 2005	8
7 Jul 2006	2 Aug 2006	26	12 Jul 2006	3 Aug 2006	22
28 Jun 2009	7 Jul 2009	9	1 Jul 2009	6 Jul 2009	5
19 Aug 2009	7 Sep 2009	19	30 Aug 2009	5 Sep 2009	6
8 Jul 2010	20 Jul 2010	12	–	–	0
14 Aug 2012	30 Aug 2012	16	16 Aug 2012	30 Aug 2012	14
19 Jul 2013	28 Jul 2013	9	–	–	0
7 Sep 2014	26 Sep 2014	19	–	–	0
29 Jun 2015	10 Jul 2015	11	–	–	0
9 Jun 2017	27 Jun 2017	18	11 Jun 2017	27 Jun 2017	16
28 Jul 2018	12 Aug 2018	15	29 Jul 2018	13 Aug 2018	15
26 Jun 2019	8 Jul 2019	12	30 Jun 2019	8 Jul 2019	8
11 Jun 2021	21 Jun 2021	10	–	–	0
6 Jun 2022	25 Jun 2022	19	–	–	0
11 Jul 2022	18 Aug 2022	38	15 Jul 2022	16 Aug 2022	32
25 Aug 2022	22 Sep 2022	28	2 Sep 2022	17 Sep 2022	15
31 May 2023	16 Jun 2023	16	–	–	0

Table A3. PC2− MHW events detected between 31 May and 26 September over the 1982–2024 period, matched with concurrent MHW events detected with the method of Section 3.4.

PC2− Start	PC2− End	PC2− Days	MHW Start	MHW End	MHW Days
23 Jun 1982	4 Jul 1982	11	24 Jun 1982	3 Jul 1982	9
5 Jun 1985	14 Jun 1985	9	8 Jun 1985	12 Jun 1985	4
11 Aug 1994	26 Sep 1994	46	3 Aug 1994	20 Sep 1994	48
14 Aug 1998	27 Aug 1998	13	–	–	0
31 May 1999	20 Jun 1999	20	31 May 1999	13 Jun 1999	13
5 Jun 2000	17 Jun 2000	12	–	–	0
28 Jul 2002	9 Aug 2002	12	30 Jul 2002	8 Aug 2002	9
14 Jun 2003	8 Jul 2003	24	4 Jun 2003	5 Sep 2003	93
31 Aug 2011	26 Sep 2011	26	8 Sep 2011	21 Sep 2011	13
29 Jun 2012	17 Jul 2012	18	1 Jul 2012	16 Jul 2012	15
20 Jul 2015	19 Aug 2015	30	15 Jul 2015	19 Aug 2015	35
28 Aug 2015	8 Sep 2015	11	31 Aug 2015	4 Sep 2015	4
31 May 2018	13 Jun 2018	13	31 May 2018	9 Jun 2018	9
16 Sep 2018	25 Sep 2018	9	7 Sep 2018	24 Sep 2018	17
17 Jul 2023	7 Aug 2023	21	12 Jul 2023	4 Aug 2023	23
13 Jul 2024	14 Sep 2024	63	13 Jul 2024	14 Sep 2024	63

References

1. Darmaraki, S.; Denaxa, D.; Theodorou, I.; Livanou, E.; Rigatou, D.; Raitsos, D.; Stavrakidis-Zachou, O.; Dimarchopoulou, D.; Bonino, G.; Mcadam, R. Marine Heatwaves in the Mediterranean Sea: A Literature Review. *Mediterr. Mar. Sci.* **2024**, *25*, 586–620. [CrossRef]
2. EU Copernicus Marine Service. Global Ocean Sea Surface Temperature Time Series and Trend from Observations Reprocessing. Available online: https://marine.copernicus.eu/access-data/ocean-monitoring-indicators/global-ocean-sea-surface-temperature-time-series-and-trend (accessed on 5 June 2025).

3. Garcia-Soto, C.; Cheng, L.; Caesar, L.; Schmidtko, S.; Jewett, E.B.; Cheripka, A.; Rigor, I.; Caballero, A.; Chiba, S.; Báez, J.C.; et al. An Overview of Ocean Climate Change Indicators: Sea Surface Temperature, Ocean Heat Content, Ocean pH, Dissolved Oxygen Concentration, Arctic Sea Ice Extent, Thickness and Volume, Sea Level and Strength of the AMOC (Atlantic Meridional Overturning Circulation). *Front. Mar. Sci.* **2021**, *8*, 642372. [CrossRef]
4. Konsta, K.; Doxa, A.; Katsanevakis, S.; Mazaris, A.D. Projected marine heatwaves over the Mediterranean Sea and the network of marine protected areas: A three-dimensional assessment. *Clim. Change* **2025**, *178*, 17. [CrossRef]
5. Coll, M.; Piroddi, C.; Steenbeek, J.; Kaschner, K.; Lasram, F.B.R.; Aguzzi, J.; Ballesteros, E.; Bianchi, C.N.; Corbera, J.; Dailianis, T.; et al. The biodiversity of the Mediterranean Sea: Estimates, patterns, and threats. *PLoS ONE* **2010**, *5*, e11842. [CrossRef] [PubMed]
6. Cappelletto, M.; Santoleri, R.; Evangelista, L.; Galgani, F.; Garcés, E.; Giorgetti, A.; Fava, F.; Herut, B.; Hilmi, K.; Kholeif, S.; et al. The Mediterranean Sea we want. *Ocean Coast. Res.* **2021**, *69*, e21031. [CrossRef]
7. Garrabou, J.; Gómez-Gras, D.; Medrano, A.; Cerrano, C.; Ponti, M.; Schlegel, R.; Bensoussan, N.; Turicchia, E.; Sini, M.; Gerovasileiou, V.; et al. Marine heatwaves drive recurrent mass mortalities in the Mediterranean Sea. *Glob. Change Biol.* **2022**, *28*, 5708–5725. [CrossRef]
8. Stipcich, P.; Apostolaki, E.T.; Chartosia, N.; Efthymiadis, P.T.; Jimenez, C.E.; La Manna, G.; Pansini, A.; Principato, E.; Resaikos, V.; Ceccherelli, G. Assessment of Posidonia oceanica traits along a temperature gradient in the Mediterranean Sea shows impacts of marine warming and heat waves. *Front. Mar. Sci.* **2022**, *9*, 895354. [CrossRef]
9. Orenes-Salazar, V.; Navarro-Martínez, P.C.; Ruíz, J.M.; García-Charton, J.A. Recurrent marine heatwaves threaten the resilience and viability of a key Mediterranean octocoral species. *Aquat. Conserv. Mar. Freshw. Ecosyst.* **2023**, *33*, 1161–1174. [CrossRef]
10. Le Grix, N.; Zscheischler, J.; Rodgers, K.B.; Yamaguchi, R.; Frölicher, T.L. Hotspots and drivers of compound marine heatwaves and low net primary production extremes. *Biogeosciences* **2022**, *19*, 5807–5835. [CrossRef]
11. Atalah, J.; Ibañez, S.; Aixalà, L.; Barber, X.; Sánchez-Jerez, P. Marine heatwaves in the western Mediterranean: Considerations for coastal aquaculture adaptation. *Aquaculture* **2024**, *588*, 740917. [CrossRef]
12. Jangir, B.; Mishra, A.K.; Strobach, E. The interplay between medicanes and the Mediterranean Sea in the presence of sea surface temperature anomalies. *Atmos. Res.* **2024**, *310*, 107625. [CrossRef]
13. Hamdeno, M.; Alvera-Azcaráte, A. Marine heatwaves characteristics in the Mediterranean Sea: Case study the 2019 heatwave events. *Front. Mar. Sci.* **2023**, *10*, 1093760. [CrossRef]
14. Choi, H.Y.; Park, M.S.; Kim, H.S.; Lee, S. Marine heatwave events strengthen the intensity of tropical cyclones. *Commun. Earth Environ.* **2024**, *5*, 69. [CrossRef]
15. Pastor, F.; Paredes-Fortuny, L.; Khodayar, S. Mediterranean marine heatwaves intensify in the presence of concurrent atmospheric heatwaves. *Commun. Earth Environ.* **2024**, *5*, 797. [CrossRef]
16. Paredes-Fortuny, L.; Pastor, F.; Khodayar, S. Concurrent atmospheric heatwaves intensify marine heatwaves through air-sea heat flux change in the Mediterranean Sea. *Commun. Earth Environ.* **2025**, *6*, 638. [CrossRef]
17. Miglietta, M.M.; Mazon, J.; Motola, V.; Pasini, A. Effect of a positive Sea Surface Temperature anomaly on a Mediterranean tornadic supercell. *Sci. Rep.* **2017**, *7*, 12828. [CrossRef]
18. Martín, M.L.; Calvo-Sancho, C.; Taszarek, M.; González-Alemán, J.J.; Montoro-Mendoza, A.; Díaz-Fernández, J.; Bolgiani, P.; Sastre, M.; Martín, Y. Major Role of Marine Heatwave and Anthropogenic Climate Change on a Giant Hail Event in Spain. *Geophys. Res. Lett.* **2024**, *51*, e2023GL107632. [CrossRef]
19. Hobday, A.J.; Alexander, L.V.; Perkins, S.E.; Smale, D.A.; Straub, S.C.; Oliver, E.C.; Benthuysen, J.A.; Burrows, M.T.; Donat, M.G.; Feng, M.; et al. A hierarchical approach to defining marine heatwaves. *Prog. Oceanogr.* **2016**, *141*, 227–238. [CrossRef]
20. Pastor, F.; Khodayar, S. Marine heat waves: Characterizing a major climate impact in the Mediterranean. *Sci. Total Environ.* **2023**, *861*, 160621. [CrossRef]
21. Darmaraki, S.; Somot, S.; Sevault, F.; Nabat, P.; Narvaez, W.D.C.; Cavicchia, L.; Djurdjevic, V.; Li, L.; Sannino, G.; Sein, D.V. Future evolution of Marine Heatwaves in the Mediterranean Sea. *Clim. Dyn.* **2019**, *53*, 1371–1392. [CrossRef]
22. Xu, T.; Newman, M.; Capotondi, A.; Stevenson, S.; Di Lorenzo, E.; Alexander, M.A. An increase in marine heatwaves without significant changes in surface ocean temperature variability. *Nat. Commun.* **2022**, *13*, 7396. [CrossRef] [PubMed]
23. Ciappa, A.C. Effects of Marine Heatwaves (MHW) and Cold Spells (MCS) on the surface warming of the Mediterranean Sea from 1989 to 2018. *Prog. Oceanogr.* **2022**, *205*, 102828. [CrossRef]
24. Smith, K.E.; Burrows, M.T.; Hobday, A.J.; King, N.G.; Moore, P.J.; Sen Gupta, A.; Thomsen, M.S.; Wernberg, T.; Smale, D.A. Biological Impacts of Marine Heatwaves. *Annu. Rev. Mar. Sci.* **2023**, *15*, 119–145. [CrossRef]
25. Rosselló, P.; Pascual, A.; Combes, V. Assessing marine heat waves in the Mediterranean Sea: A comparison of fixed and moving baseline methods. *Front. Mar. Sci.* **2023**, *10*, 1168368. [CrossRef]
26. Martínez, J.; Leonelli, F.E.; García-Ladona, E.; Garrabou, J.; Kersting, D.K.; Bensoussan, N.; Pisano, A. Evolution of marine heatwaves in warming seas: The Mediterranean Sea case study. *Front. Mar. Sci.* **2023**, *10*, 1193164. [CrossRef]
27. Denaxa, D.; Korres, G.; Bonino, G.; Masina, S.; Hatzaki, M. The role of air–sea heat flux for marine heatwaves in the Mediterranean Sea. *State Planet* **2024**, *4-osr8*, 11 [CrossRef]

28. Bonino, G.; McAdam, R.; Athanasiadis, P.; Cavicchia, L.; Rodrigues, R.R.; Scoccimarro, E.; Tibaldi, S.; Masina, S. Mediterranean summer marine heatwaves triggered by weaker winds under subtropical ridges. *Nat. Geosci.* **2025**, *18*, 848–853. [CrossRef]
29. Darmaraki, S.; Somot, S.; Sevault, F.; Nabat, P. Past variability of Mediterranean Sea marine heatwaves. *Geophys. Res. Lett.* **2019**, *46*, 9813–9823. [CrossRef]
30. Huang, B.; Liu, C.; Banzon, V.; Freeman, E.; Graham, G.; Hankins, B.; Smith, T.; Zhang, H.M. Improvements of the Daily Optimum Interpolation Sea Surface Temperature (DOISST) Version 2.1. *J. Clim.* **2021**, *34*, 2923–2939. [CrossRef]
31. Hersbach, H.; Bell, B.; Berrisford, P.; Hirahara, S.; Horányi, A.; Muñoz-Sabater, J.; Nicolas, J.; Peubey, C.; Radu, R.; Schepers, D.; et al. The ERA5 global reanalysis. *Q. J. R. Meteorol. Soc.* **2020**, *146*, 1999–2049. [CrossRef]
32. Juza, M.; Fernańdez-Mora, A.; Tintoré, J. Sub-Regional Marine Heat Waves in the Mediterranean Sea From Observations: Long-term Surface Changes, Sub-Surface and Coastal Responses. *Front. Mar. Sci.* **2022**, *9*, 785771. [CrossRef]
33. Cleveland, R.B.; Cleveland, W.S.; McRae, J.E.; Terpenning, I. STL: A seasonal-trend decomposition. *J. Off. Stat.* **1990**, *6*, 3–73.
34. Seabold, S.; Perktold, J. statsmodels: Econometric and statistical modeling with python. In Proceedings of the 9th Python in Science Conference, Austin, TX, USA, 28 June–3 July 2010.
35. Denaxa, D.; Korres, G.; Flaounas, E.; Hatzaki, M. Investigating extreme marine summers in the Mediterranean Sea. *Ocean Sci.* **2024**, *20*, 433–461. [CrossRef]
36. Yu, L. Sea Surface Exchanges of Momentum, Heat, and Freshwater Determined by Satellite Remote Sensing. In *Encyclopedia of Ocean Sciences*; Elsevier: Amsterdam, The Netherlands, 2019; pp. 15–23. [CrossRef]
37. Rieger, N.; Levang, S.J. xeofs: Comprehensive EOF analysis in Python with xarray. *J. Open Source Softw.* **2024**, *9*, 6060. [CrossRef]
38. Joseph, L.; Skliris, N.; Dey, D.; Marsh, R. Drivers and Variability of Marine Heatwaves in the North Indian Ocean and their Impacts on South Asian Monsoon Rainfall. *EGUsphere* **2025**, *preprint*. [CrossRef]
39. Skliris, N.; Marsh, R.; Breedon, M.; Josey, S.A. Accelerated Warming and Salinification of the Mediterranean Sea: Implications for Dense Water Formation. *J. Mar. Sci. Eng.* **2024**, *13*, 25. [CrossRef]
40. Simon, A.; Plecha, S.M.; Russo, A.; Teles-Machado, A.; Donat, M.G.; Auger, P.A.; Trigo, R.M. Hot and cold marine extreme events in the Mediterranean over the period 1982–2021. *Front. Mar. Sci.* **2022**, *9*, 892201. [CrossRef]
41. Dayan, H.; McAdam, R.; Juza, M.; Masina, S.; Speich, S. Marine heat waves in the Mediterranean Sea: An assessment from the surface to the subsurface to meet national needs. *Front. Mar. Sci.* **2023**, *10*, 1045138. [CrossRef]
42. Garrabou, J.; Coma, R.; Bensoussan, N.; Bally, M.; Chevaldonné, P.; Cigliano, M.; Diaz, D.; Harmelin, J.G.; Gambi, M.C.; Kersting, D.K.; et al. Mass mortality in Northwestern Mediterranean rocky benthic communities: Effects of the 2003 heat wave. *Glob. Change Biol.* **2009**, *15*, 1090–1103. [CrossRef]
43. Chimienti, G.; Tursi, A.; Maiorca, M.; Mastrototaro, F. Flowering of *Posidonia oceanica* in the Italian Adriatic Sea following the 2024 marine heatwave. *Estuar. Coast. Shelf Sci.* **2025**, *324*, 109483. [CrossRef]
44. Ren, J.; Wang, C.; Yao, Y. Spatiotemporally Continuous Marine Heatwaves: A Novel Clustering Approach Reveals Increasing Frequency, Duration, Area, Intensity, and Movement Distance. *Geophys. Res. Lett.* **2025**, *52*, e2024GL113211. [CrossRef]
45. Scannell, H.A.; Cai, C.; Thompson, L.; Whitt, D.B.; Gagne, D.J.; Abernathey, R.P. Spatiotemporal Evolution of Marine Heatwaves Globally. *J. Atmos. Ocean. Technol.* **2024**, *41*, 1247–1263. [CrossRef]
46. Olita, A.; Sorgente, R.; Natale, S.; Gaberšek, S.; Ribotti, A.; Bonanno, A.; Patti, B. Effects of the 2003 European heatwave on the Central Mediterranean Sea: Surface fluxes and the dynamical response. *Ocean. Sci.* **2007**, *3*, 273–289. [CrossRef]
47. Sen Gupta, A.; Thomsen, M.; Benthuysen, J.A.; Hobday, A.J.; Oliver, E.; Alexander, L.V.; Burrows, M.T.; Donat, M.G.; Feng, M.; Holbrook, N.J.; et al. Drivers and impacts of the most extreme marine heatwave events. *Sci. Rep.* **2020**, *10*, 19359. [CrossRef]
48. Simon, A.; Pires, C.; Frölicher, T.L.; Russo, A. Long-term warming and interannual variability contributions' to marine heatwaves in the Mediterranean. *Weather Clim. Extrem.* **2023**, *42*, 100619. [CrossRef]
49. Vijaykumar, P.; Abhilash, S.; Santhosh, K.; Mapes, B.; Suvarchal Kumar, C.; Hu, I.K. Distribution of cloudiness and categorization of rainfall types based on INSAT IR brightness temperatures over Indian subcontinent and adjoining oceanic region during south west monsoon season. *J. Atmos. Sol.-Terr. Phys.* **2017**, *161*, 76–82. [CrossRef]
50. Androulidakis, Y.; Krestenitis, Y. Sea surface temperature variability and marine heat waves over the Aegean, Ionian, and Cretan Seas from 2008–2021. *J. Mar. Sci. Eng.* **2022**, *10*, 42. [CrossRef]
51. Saçu, Ş.; Şen, O.; Erdik, T.; Öztürk, İ. Sea surface temperature and marine heatwave variability in interconnected basins: The Black-Marmara-Aegean Seas. *Dyn. Atmos. Ocean.* **2025**, *110*, 101555. [CrossRef]
52. Bian, C.; Jing, Z.; Wang, H.; Wu, L. Scale-Dependent Drivers of Marine Heatwaves Globally. *Geophys. Res. Lett.* **2024**, *51*, e2023GL107306. [CrossRef]